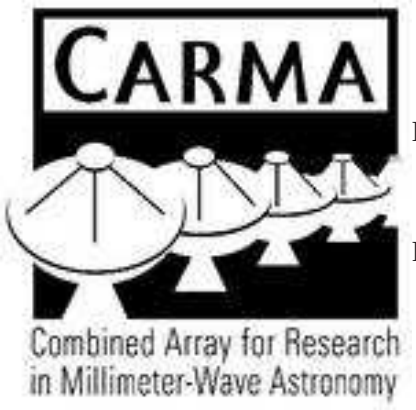


CARMA Memorandum Series #53

# CARMA SUMMER SCHOOL 2009

Melvyn Wright, Marc Pound, Dick Plambeck, John Carpenter, Nikolaus Volgenau, Douglas Bock, Chat Hull, Statia Luszcz Cook, Adam Morgan, M. Nurur Rahman, Shaye Storm, Rui Xue, David Andres Rebolledo Lara, Jonathan Seale, Alissa Bans, Reid Sherman, Alexandra Lockwood, Shriharsh Tendulkar, Tucker Jones, Lee Rottler, Gul Esra Bulbul, Laura Lopez, Kate Barnes, Joanna Bulger, Nazirah Jetha

August 19, 2009

## ABSTRACT

The third CARMA Summer School was held at the observatory on Cedar Flat 2009 July 12-18 with 19 students from Berkeley, Caltech, Illinois, Maryland, U. Chicago, U of Alabama, UC Santa Cruz, Indiana U, and U of Exeter. During the school each participant made observations of everything from a comet to a GRB, analyzed and presented the results. In this memo we collect together some of the results from the student projects.

## 1. Introduction

The third CARMA Summer School was held at the observatory on Cedar Flat 2009 July 12-18 with 19 students from Berkeley, Caltech, Illinois, Maryland, U. Chicago, U of Alabama, UC Santa Cruz, Indiana U, and Exeter.

The school had the use of the telescope for the week. The array was in the compact E-configuration. During the school the students had their own observing projects which they worked on during the week as well as attending lectures and demonstations. Each of the student projects had 5-6 hours of telescope time and the students controlled the telescope for their own projects. The students took the observations, reduced the data, analyzed and presented the results.

On Monday the students learned how to select suitable observing projects for the CARMA telescope. The introductory lectures covered the characteristics of the telescope, instrumentation, and observing techniques. The students learned how to:
1) select suitable astronomical sources for observating.
2) select the observing frequency, spectral lines to be observed.
3) evaluate angular resolution, velocity resolution and sensitivity needed.
4) select the correlator setup and calibrations needed.
5) prepare an observing script to define the observing procedure at the telescope.
6) make the observations

During the rest of the week, the lectures and demonstrations covered the theory and techniques used for millimeter wavelength aperture synthesis and the CARMA array. As they worked on their projects the students learned how to:
7) schedule the telescope effectively.
8) calibrate the data.
9) make images.
10) identify and fix problems that set off the alarm.
11) analyze and present the results.

On Friday the students made 10-15 minute presentations and we discussed the results. In all, a very satisfying week seeing all the enthusiasm and so many exciting projects from initial planning and observations, to analysis and results.

Students got an example of dealing with major problem when the diesel generators failed on Monday afternoon. (This led to an impromptu tour of the generators since no hearing protection would be required). The staff worked diligently and restored stable power after a few hours, as well as restarting the correlators, so by evening observations could proceed.

## 2. The CARMA Telescope

The CARMA telescope is designed as an aperture synthesis telescope. There are two receiver bands: 3 mm and 1 mm. A basic aperture synthesis observation makes an image the size of the primary beam ($\lambda/D \sim 1'$ at 100 GHz; $0.5'$ at 230 GHz) with a resolution corresponding to the maximum separations of the 15 antennas. You will learn how this works at the school. During the school, the telescope was in a compact antenna configuration, the D-configuration, which gives an angular resolution of $\sim$3-6 at 100 GHz, and 1.5-3$''$ at 230 GHz.

The most convenient source size is one which is smaller than the size of the primary beam when only one pointing is needed. Larger sources can be imaged by time-sharing the pointing of the antennas (mosaicing), at the cost of lowered sensitivity.

The sensitivity is determined by the system noise (receivers plus atmosphere), the bandwidth (or velocity resolution), and the observing time. The atmosphere is usually not so good for 1 mm observations in the summer, or for sources which are at low declinations and must be observed through more of the atmosphere, so it's best to select a bright source which is high in the sky and can be observed at 3 mm, It's best to observe a strong enough source that we can make an image during the school, rather than a detection project, then we can see the effects of different imaging techniques.

Some of the projects that the students wanted to do did not satisfy all these conditions. We put the data on disk where it could be reduced by multiple students, so we could compare the results using different data reduction methods, and the students could work on different types of projects (single pointing, mosaics, continuum, spectral line etc.)

A technical description of the array is at *http://cedarflat.mmarray.org/observing/doc/instrument_desc.html* and there are tools to calculate sensitivity, visualize the correlator setup, and locate bright calibration sources at *http://cedarflat.mmarray.org/observing/tools* .

### 2.1. Logistics

Because this is a 'hands-on' school, all lectures and demonstrations were held in the control building and at the telescopes at Cedar Flat. Mel, Marc, Dick and 11 of the students stayed in the 'Nelson' group campground, about 1.5 miles from the control room, and near the antenna pads for the A-configuration. Those who camped avoided the hassle of driving up and down the mountain each day (made significantly more lengthy by CalTrans road repaving), and had a wonderful opportunity to star-gaze each night. The other students stayed in the dorm and cottage at OVRO. Delicious breakfast, lunch, and dinners were provided at the observatory, prepared by Terry Sepsey and Cecil Patrick. We organized a hike up Big Pine Creek to Sam Mack Meadow on Saturday 18 July.

## 3. Reid Sherman (University of Chicago), Alexandra Lockwood (CalTech), and Statia Luszcz Cook (University of California at Berkeley)

The process of high-mass star formation plays and important role in galactic dynamics and chemistry and is still not well understood. Accretion rates and luminosity constraints prohibit massive stellar objects from forming in the same manner as low-mass stars and may indicate a multiple-core synthesis. The fact that high-mass stars only form in clusters and interact in complex feedback loops with their environment make them difficult to study but also very interesting. However, the combination of cold dust, outflows, and shocked molecular gas allows these regions to be studied in multiple wavelengths.

IRAS20188+3928 (aka Mol121) is a protostellar region in Cygnus X that has been detected from near-IR to centimeter wavelengths. Continuum emission has indicated a significant mass of cool dust in dense clumps (Curran & Chrysostomou, 2008). Meanwhile, molecular line observations give evidence of CO outflows and H20 masers in this same condense region (Jenness et al, 1995, Schneider et al, 2006). Recent measurements at 850 um have also exhibited polarization of the dust that can be used to map the magnetic fields of the clump (Curran & Chysostomou, 2008). All of these observations reveal clues as to the evolutionary morphology of this massive protostellar cluster. Because of the high submillimeter continuum flux indicating previously unresolved structure and the dearth of observations at longer wavelengths, we believe Mol121 is a good candidate for CARMA observations at 3mm.

We observed Mol121 with the CARMA E-configuration at 100 Ghz from approximately 4 to 12 UT on July 14, 2009 with 6 hours of integration on the source. The optimal weather conditions allowed for good signal to noise and the object's declination allowed for optimal uv coverage. We used the stable quasar 2007+404 for phase calibration which was within a few degrees of our radio source. Our passband calibrator was the quasar 2232+117. Only 14 of the telescopes were included in the observations due to a temperature malfunction with antenna 6.

Figure 1 shows the map of the source with the beam size overlayed. Despite the compact configuration of the telescopes, we are able to resolve between 3-4 separate structures, perhaps corresponding to protostellar cores. The integrated flux of the entire region is 0.31 Jy, with 85% of the contribution from the largest clump. Gaussian fits to each of the defined cores separately gives integrated fluxes of 0.26 Jy, 0.053 Jy, and 0.066Jy, working clockwise from the largest core. The maximum intensity in the region is approximately $8.8\times\ 10^{-4}$ Jy/arcsec$^2$. Figure 2 shows the map of the cleaned image and its residuals, demonstrating the strength of 2 of the clumps.

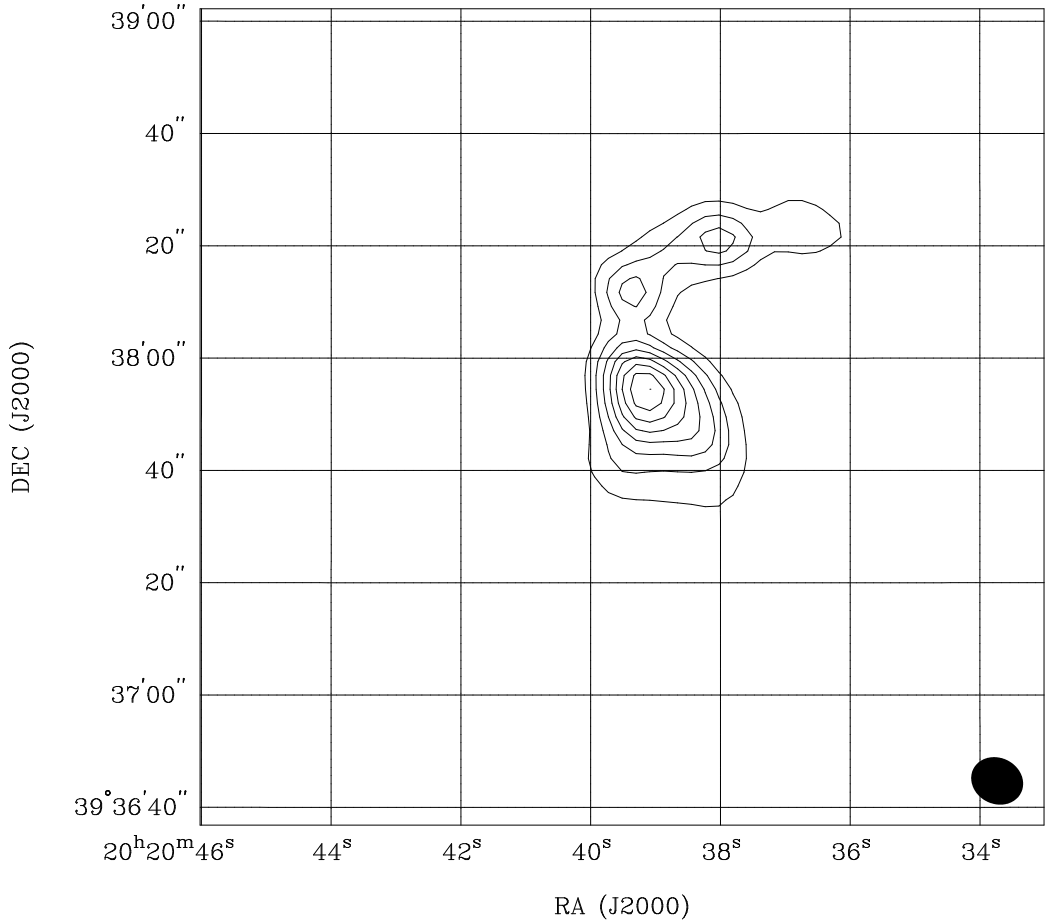


Fig. 1.— The source at 3mm with contour levels from –.0086 to 0.069 Jy/beam. The size of the beam is shown in the lower left corner.

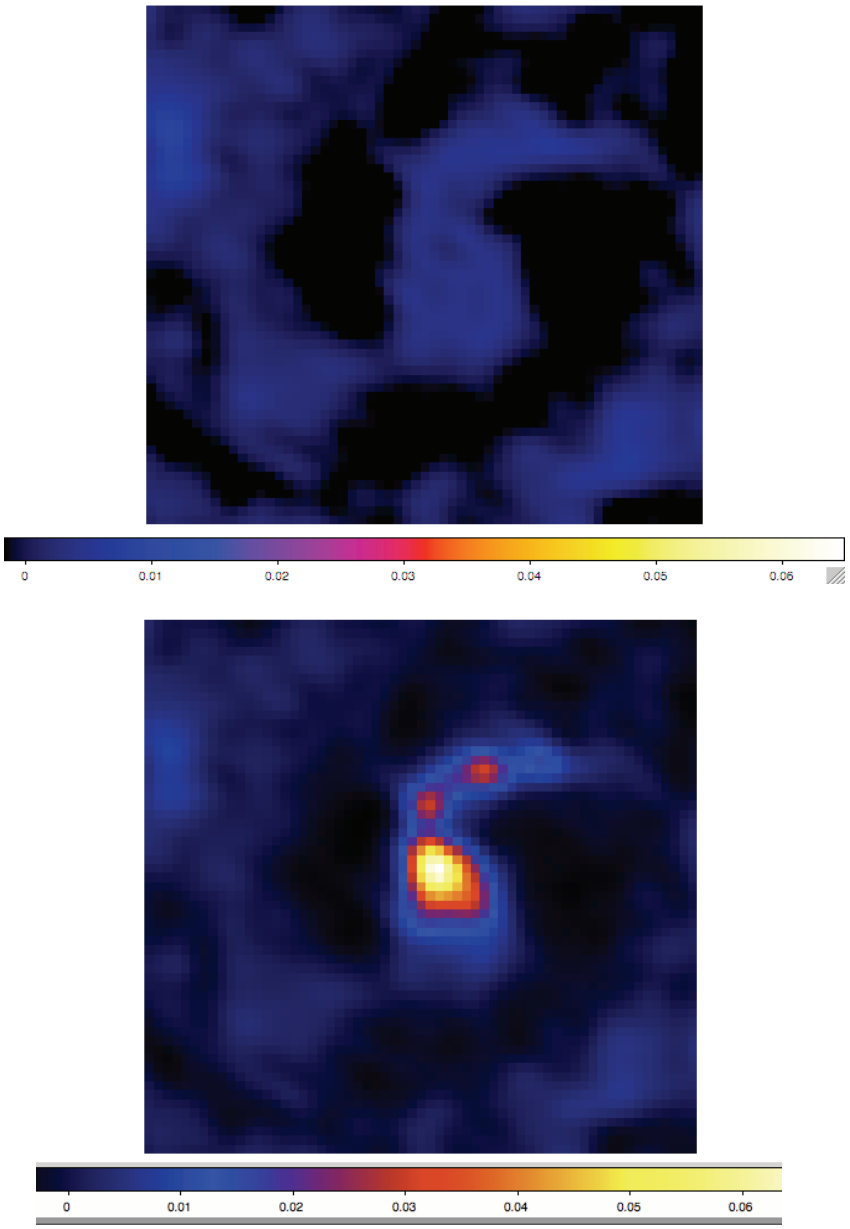


Fig. 2.— The top plot shows the residuals after the MosSDI routine is performed on the data. The bottom maps is a color image of the source which easily shows the relative strength of each of the cores. Units on the scale bars are in Jy/beam.

## 4. Chat Hull (University of California, Berkeley) & Shriharsh Tendulkar (California Institute of Technology)

### 4.1. Introduction

We used the CARMA E configuration to observe the central region of M82 in the $^{12}$CO(J=1-0) line and in a neighboring continuum region at about 114 GHz. Our aim was to create a velocity profile of the region for comparison with Olofssen & Rydbeck (1984) and a continuum map for comparison with Carlstrom & Kronberg (1991).

We configured the correlator bands to have two 62 MHz-wide windows and one 500 MHz-wide window. We set the two 62 MHz windows to flank the redshifted CO line, and overlapped three of their 980 kHz channels. The 500 MHz window was set in the continuum at frequencies below 115 GHz.

### 4.2. Results & Discussions

We created both a continuum map and a $^{12}$CO map of M82's central region. Figure 3 shows a cigar-shaped structure consistent with the optical image of M82 [Figure 4], although the structure in radio continuum is about 50 arcsec in diameter, whereas the optical galaxy has a size of 10 arcmin. The CO emission contours are overlaid on the continuum, and exhibit emission peaks in the two lobes. The double-lobed structure is suggestive of a perturbed disk. We shall see from the velocity maps that the structure is indeed rotating as a uniform disk. The high intensity in the lobes and low central intensity is suggestive of a rotating ring rather than a rotating disk.

Figure 5 shows the velocity moment map with radial velocities ranging from 70 km s$^{-1}$ (blue) to 370 km s$^{-1}$ (red). The overlaid contours show the velocity dispersion. The disk structure has a systemic recessional velocity of 220 km s$^{-1}$, the bottom right part of the structure is blueshifted (in the center of mass frame) and the upper left is redshifted. The velocity dispersion peaks in the center of the disk, which is consistent with the known outflow of gas perpendicular to the plane of the disk.

Figure 6 shows the outflow regions overlaid on the radial velocity map. The peak of the velocity dispersion corresponds with the peak of the outflow emission, which is consistent with the idea that a turbulent outflow would have a much higher velocity dispersion than a disk of coherently rotating gas.

Figure 7 shows the spectra measured at the center of the galaxy and at the two lobes. It clearly shows the velocity difference between the two lobes, and depicts the increased velocity dispersion and decreased emission intensity in the central region.

Figure 8 shows the position-velocity map of a cut along the plane of the disk. We can see that the velocity varies linearly as a function of radius from the center. This is expected in a uniformly rotating disk; however, the Keplerian velocity profile would vary as the inverse square root of the radius. One possible interpretation is that the disk is optically thick, and while the gas near the inner parts of the disk may be rotating with

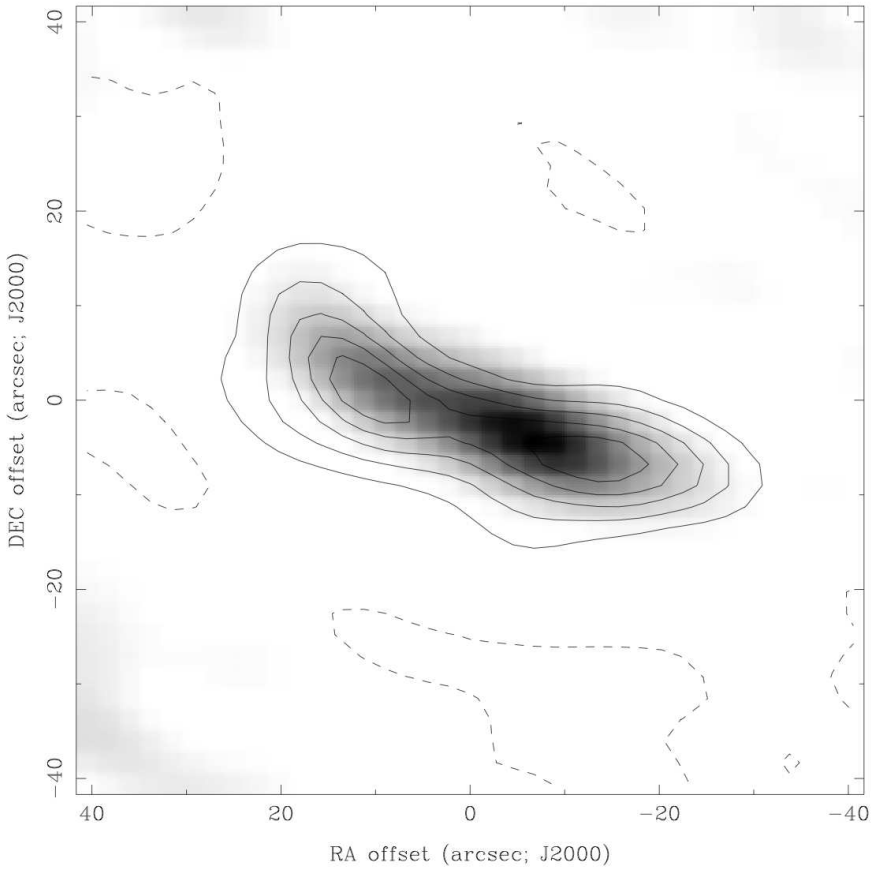


Fig. 3.— Continuum map of M82, with CO contours overlaid. The contours range from 0.4 to 2.4 Jy, with steps of 0.4 Jy

Fig. 4.— Optical image of M82. Credit: NASA, ESA, The Hubble Heritage Team, (STScIAURA.)

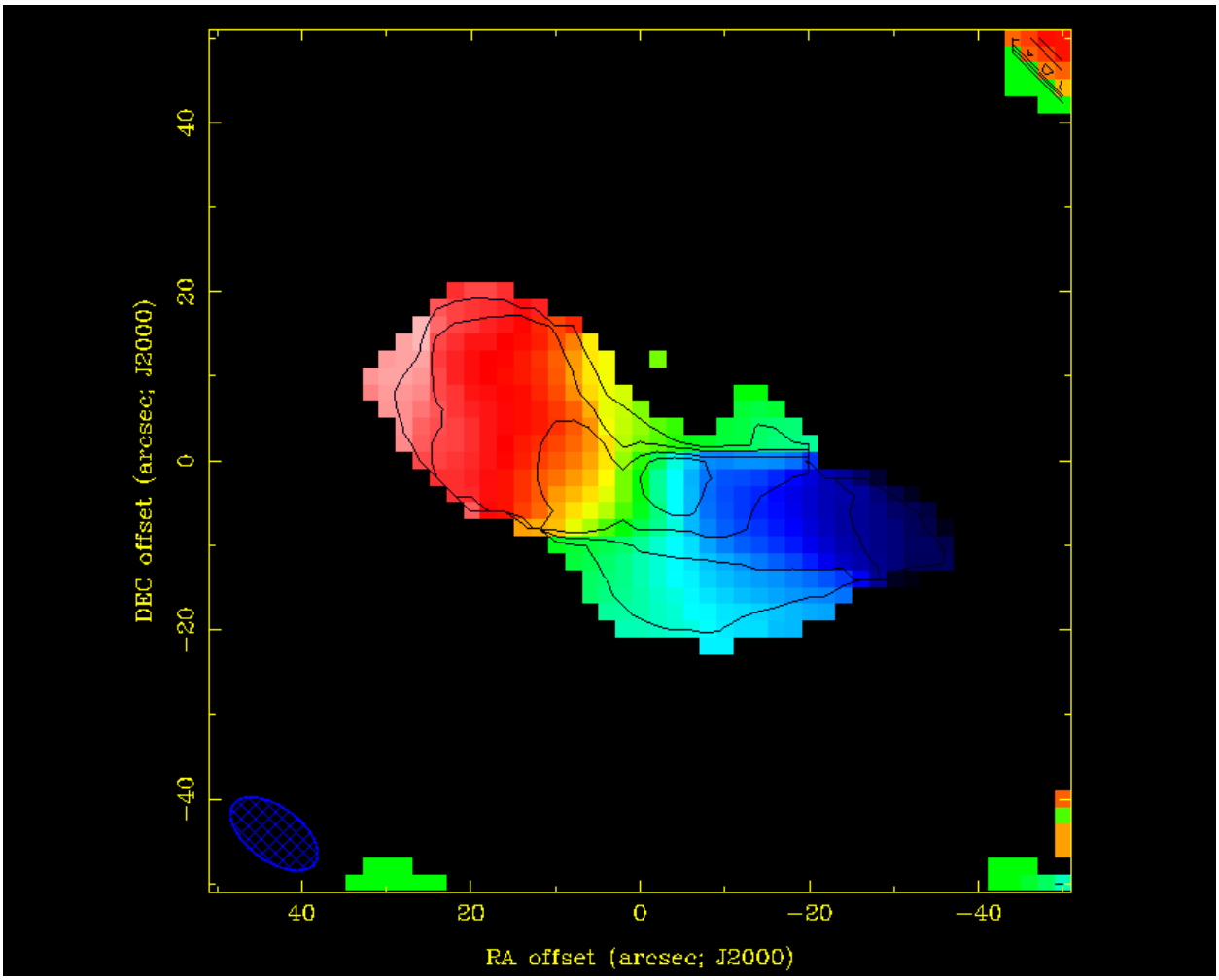


Fig. 5.— Velocity map of M82. The color scale goes from 70 km $s^{-1}$(blue) to 370 km $s^{-1}$(red). The overlayed contours are velocity dispersions with contours at 10, 20, 30, and 40 km $s^{-1}$.

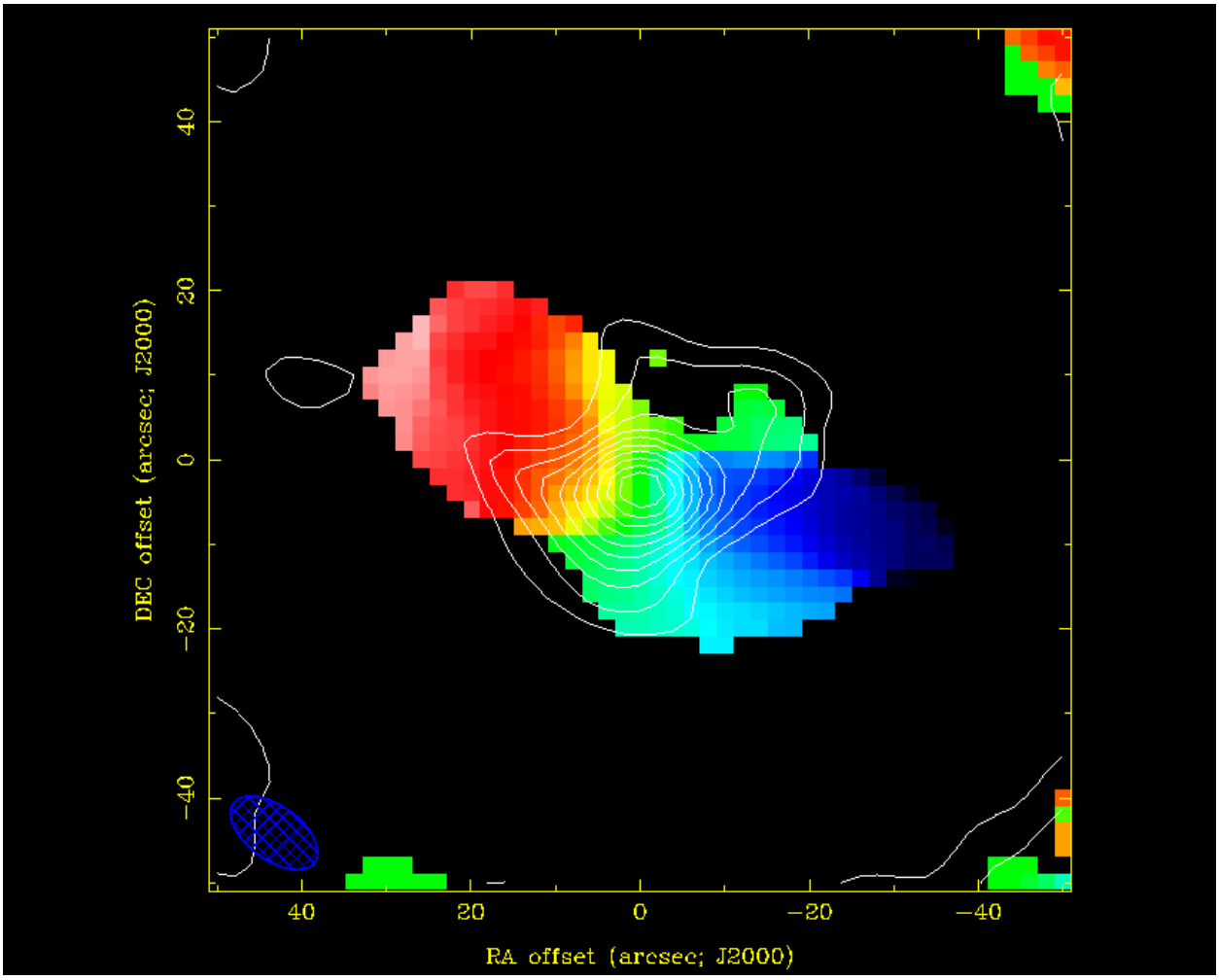


Fig. 6.— Velocity map of M82 overlayed with contours of the outflow emission.

Keplerian velocities, we are only observing the disk's outer layers.

The linearity of the position-velocity plot suggests that there is no radial outflow along our line of sight. The presence of such an outflow would create a concavity in the plot towards lower velocity.

The velocity at the peak of the CO map is $\sim$ 95 km s$^{-1}$near the disk center. The disk's radius is $\sim$25″, corresponding to 500 pc at a distance of 4.5 Mpc. If we take this to be a Keplerian orbital velocity, we estimate the disk's central mass to be $\sim 10^9\ M_\odot$. This is extremely high compared with the few-million-solar-mass black holes at the center of typical disk galaxies.

### 4.3. Conclusion

We have created a map of the central region of M82 at 115 GHz. It seems to be a disk-shaped structure of about 50 arcsec in diameter rotating with an edge velocity of $\sim$ 100km s$^{-1}$relative to the disk's rest frame. The galaxy has a systemic recessional velocity of 220 km s$^{-1}$. The existence of a radial outflow in our line of sight is unlikely considering the linearity of the position-velocity plot. The gas outflow perpendicular to the disk is consistent with the outflow seen in optical images. The rotational velocity of the disk leads to a surprisingly large dynamical mass of $10^9\ M_\odot$ within the 500 pc radius.

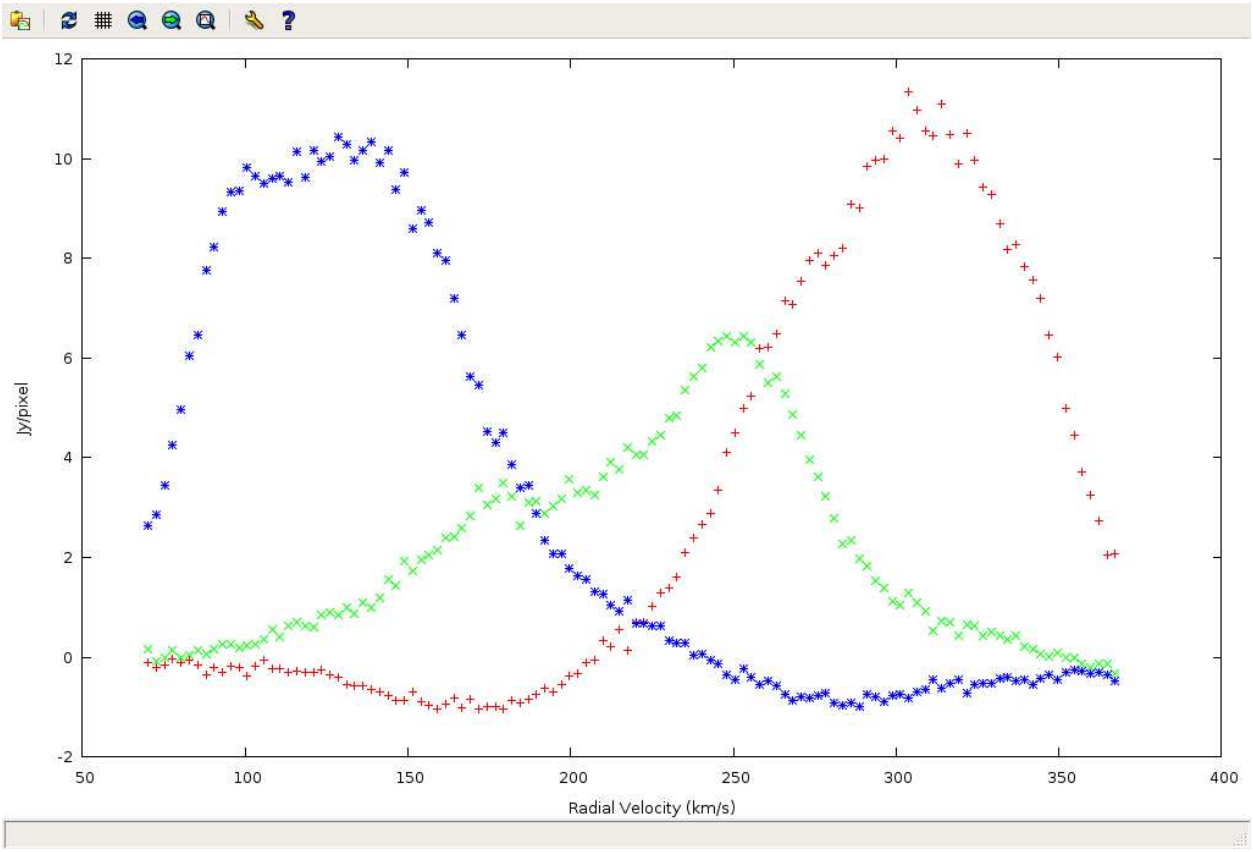


Fig. 7.— The spectra at three points in the map: one point at each lobe and one at the disk center.

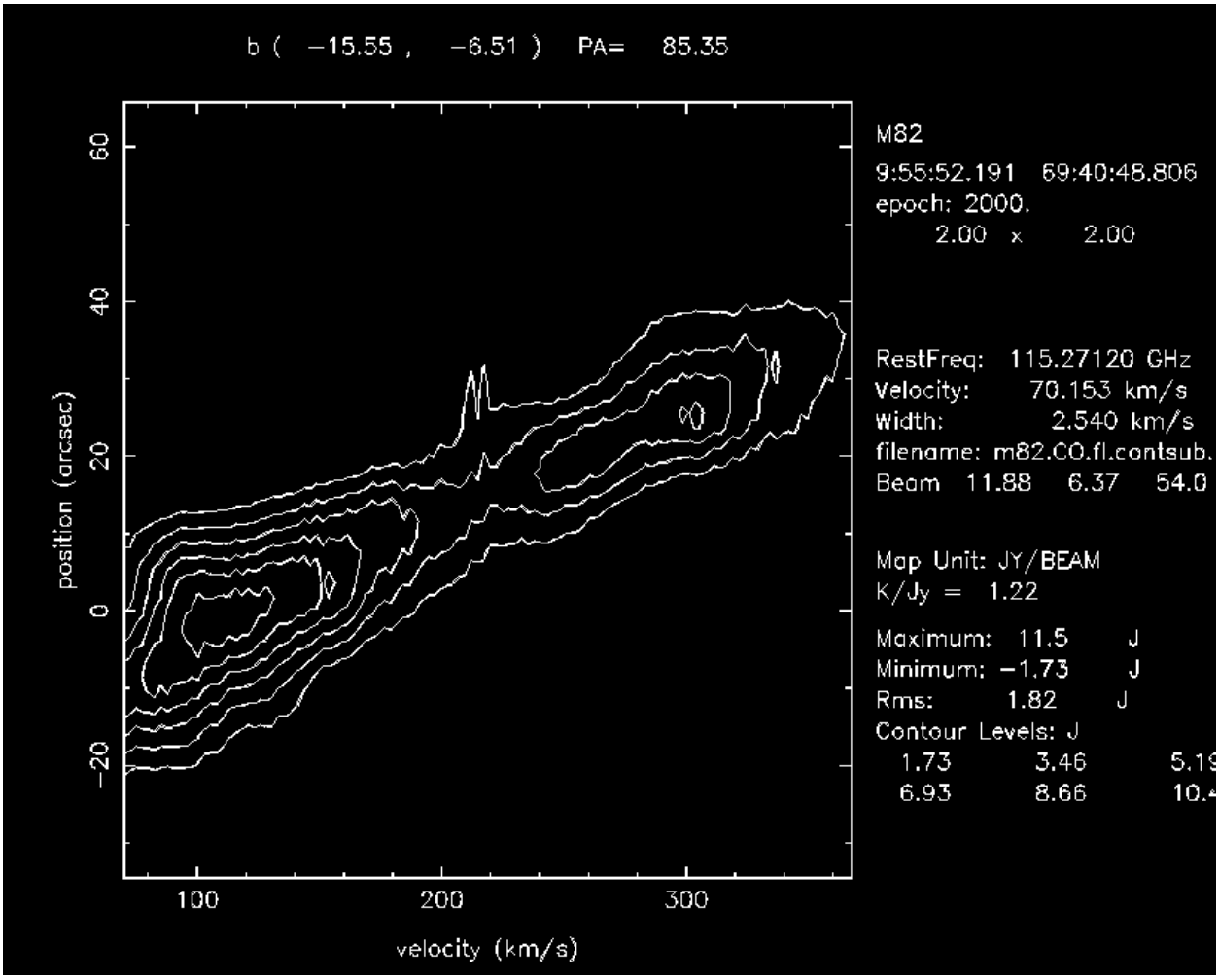


Fig. 8.— Velocity map of M82 overlaid with contours of the outflow emission.

## 5. Nazirah Jetha (Univ. of Alabama)

Galaxy groups and clusters have a well known X-ray 'cooling problem' – the X-ray emitting gas should show signs of very cold gas, which is not seen (e.g. Peterson et al 2001, Sakelliou et al 2002). Radio galaxies, which are relativistic, accretion-driven, electrically-neutral, magnetically-confined outflows from active galactic nuclei (AGN), have been posited as a possible source of heating. They can inject more than sufficient energy into the intra-cluster medium (IGM) and are cyclic in nature giving the possibility that once the IGM is no longer cooling, the radio galaxy could shut off until it is restarted due to an accumulation of cold gas. Whilst this is an appealing scenario, there are two major unknowns – firstly the actual energy content of a radio galaxy, which is dependent on its particle content, and secondly the age of any given radio source. The first problem can be addressed using a combination of low frequency ($< 1$ GHz) observations of the synchrotron emission from the radio galaxy and X-ray observations of the inverse Compton (IC) emission; the former constrains the number of radiating particles whilst the latter places limits on the total number of particles. The age of a given radio source is much more difficult to ascertain; in certain systems, where young radio sources are driving shocks into the X-ray emitting medium, ages can be determined accurately (see for example Jetha et al 2008), but this cannot obviously be done for all systems and is useless for systems where there is sustained, on-going activity. Fortunately, for a synchrotron emitting plasma with only one episode of electron acceleration, the timescale on which electrons lose energy, $\tau \propto E^{-1}$, where $E$ is the energy of the electron. This implies that higher energy (frequency) electrons lose energy faster than lower frequency electrons, meaning that high-frequency observations of radio galaxies can be used to constrain the age the plasma, assuming a given spectral aging model (e.g. Jaffe & Perola 1973). The availability of data from m to cm and mm wavelengths means that deviations from the models can be easily determined, and in the cases where such deviations are found, information can be gleaned on the injection of high energy electrons in the source.

Hardcastle & Looney (2008), have studied field radio galaxies at high frequencies and are able, with the aid of the high frequency results, to place limits on the ages of field radio sources, but no such attempt has been made with cluster radio sources. In Fig. 9 we present preliminary images of one cluster radio source, 3465, at 30 and 90 GHz, using SZA and CARMA respectively In both cases, the jet termination points can be seen, and at 30 GHz some emission from the long radio plumes can be seen. In Fig. 10 we present preliminary spectral index maps of 3C465 between 90 and 8 GHz, 30 and 8 GHz and 90 and 30 GHz, overlaid with 1.4 GHz VLA contours to show the shape and features of the source at low frequency. In each case, the jet termination points are seen as steep-spectrum, compact features, whilst the core is detected as a compact, flat-spectrum feature. With CARMA, we detect the core with a peak flux of 0.10 Jy beam$^{-1}$ compared to the rms noise level of 0.4 Jy beam$^{-1}$. The jet termination points are detected at a much lesser significance, but are still clearly visible. The plumes, when detected, are significantly steeper than the jet termination points, indicative of the plasma not being re-accelerated. Comparison with the low frequency spectral maps (Fig, 10), shows significant spectral steepening at high frequencies, qualitatively consistent with the spectral aging models of Jaffe & Perola (1973). However, this needs to be confirmed numerically, and further work will focus on making accurate determinations of the flux in different parts of the radio source at all frequencies and using these flux determinations to test existing spectral aging models.

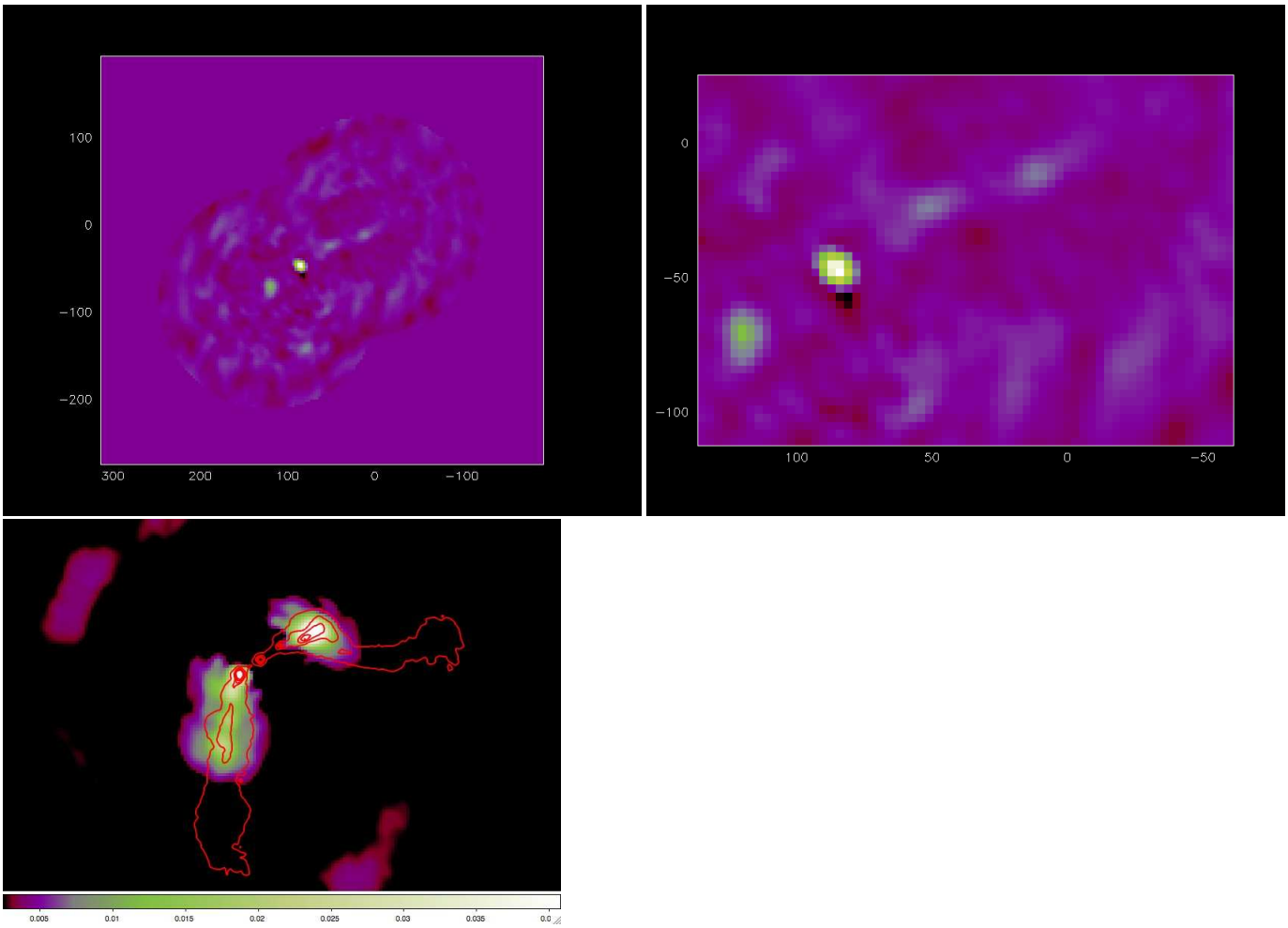


Fig. 9.— 90 GHz CARMA (top) and 30 GHz SZA (bottom) images of the radio source 3C465, with 1.4GHz VLA radio contours overlaid on the SZA image. In each image the core and jet termination points are visible, and the plume is detected at 30 GHz.

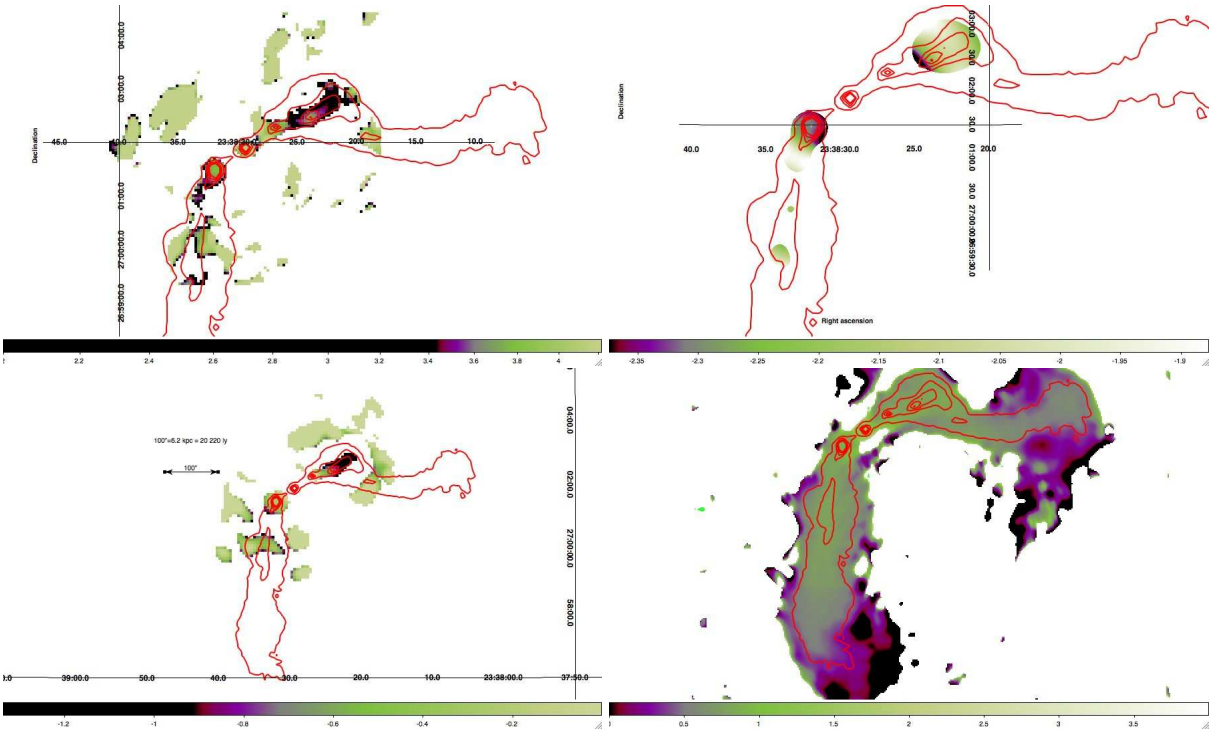


Fig. 10.— Spectral index maps between 90 and 8 GHz (top left), 30 and 8 GHz (top right), 90 and 30 GHz (bottom left) and 1.4 and 0.330 GHz (bottom right), each overlaid with the 1.4 GHz VLA contours. In each of the first three maps the jet termination points are detected as steep-spectrum compact features, and where the lobes are detected, they are significantly steeper than in the low frequency spectral index map.

## 6. David Rebolledo (University of Illinois at Urbana Champaign)

### 6.1. Science goals

Our goal is to determine whether azimuthal segregation of various gas and star formation tracers will occur in non grand-design galaxies (spiral galaxies with non well defined arms). I proposed to map the CO emission in the eastern part of nearby non grand-design spiral galaxy NGC 6946. Taking advantage of its proximity, low inclination and strong CO emission, as well as access to high quality datasets at variety of wavelenghts, I will make a high spatial resolution study of the gas distribution in this part of the galaxy and star formation tracers, which might indicate a temporal sequence of molecular cloud and star formation evolution.

### 6.2. Observation set up

Observation was taken using the E array configuration at CARMA telescope. A 49 pointing mosaic map was obtained in a 4.6 hours track, 2.9 over the source. The correlator was set to observe $^{12}$CO(1→0) line using two overlapping windows (31 MHz wideband) and one wide 500 MHz window in the USB, and to observe $^{13}$CO(1→0) in the LSB uisng the same window configuration. Figure 11 shows the coverage in the UV plane during the observation. The offsets of the 49 pointings were given respect to the center of the galaxy in order to expand the observation to other regions on the disk on future observations. During the track, antenna 2 showed bad amplitude and phase data, so was flagged during calibration procedure.

### 6.3. Calibration and Results

In order to have good results, I had to flag data from antenna 2, 7 and 8. Signal to noise in bandpass calibrator was low, so I must apply the passband autocorrelation method to calibrate the data. Further data examination showed that windows 3 and 5 in antenna 5 and 6 must be flagged also. Figure 12 shows the final integrated map for $^{12}$CO(1→0) emission in the eastern part of NGC 6946 using black-white scale and a contour map. Contours start at 3 $\sigma$ level ($\sigma$=0.34 Jy/beam km/s). Flux calibration was not applied to generate this map. The resulting beam size was 17 arcsec $\times$ 3 arcsec, with a position angle of 19.6 deg. Figure 13 shows the same contour $^{12}$CO map shown in Figure 12, overlaid on a HI image from THINGS (The HI Nearby Galaxy Survey) from VLA. The edge of the mosaic was not removed to show the extension of the map in the disk. Clearly we can see that the distribution of the molecular gas is located on the spiral arms, where HI atomic gas shows peaks also. HI gas is more extended (between the arms, and in outter regions), somethig expected because molecular gas traces regions of dense gas. Probably molecular gas, in non grand design multiarm galaxies, also traces the potential minimum. Massive Molecular gas clouds are located where former spiral arms have collided.

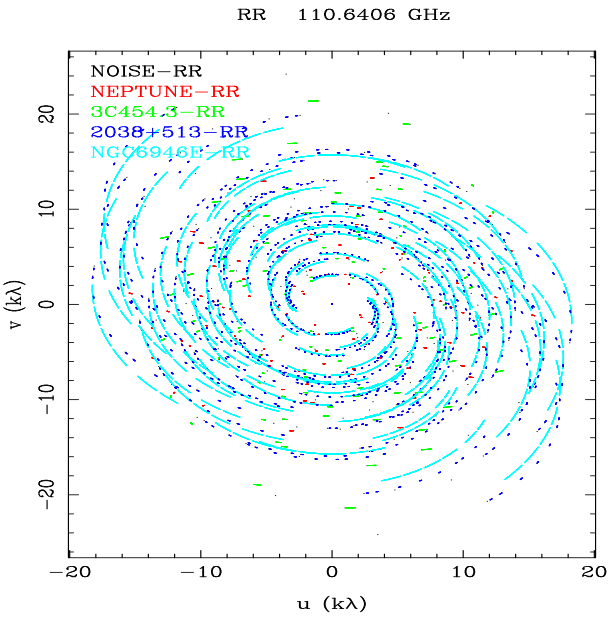


Fig. 11.— UV coverage for NGC 6946 observation.

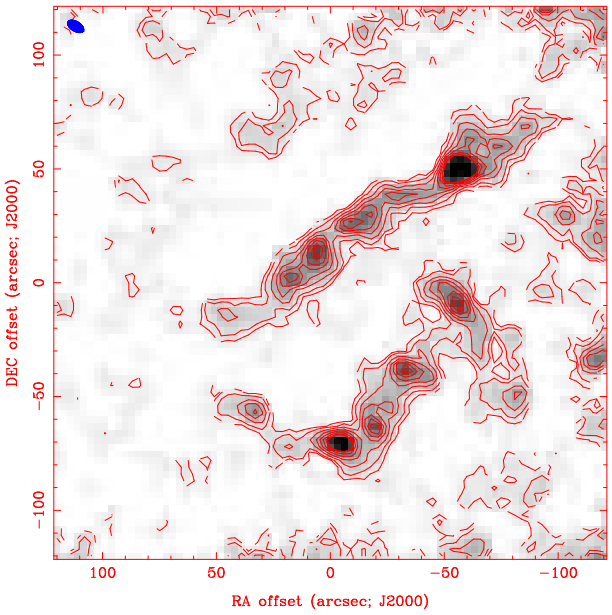


Fig. 12.— The eastern region of NGC 6946. Contours start at 3 σ level (σ = 0.34 Jy/beam km/s).

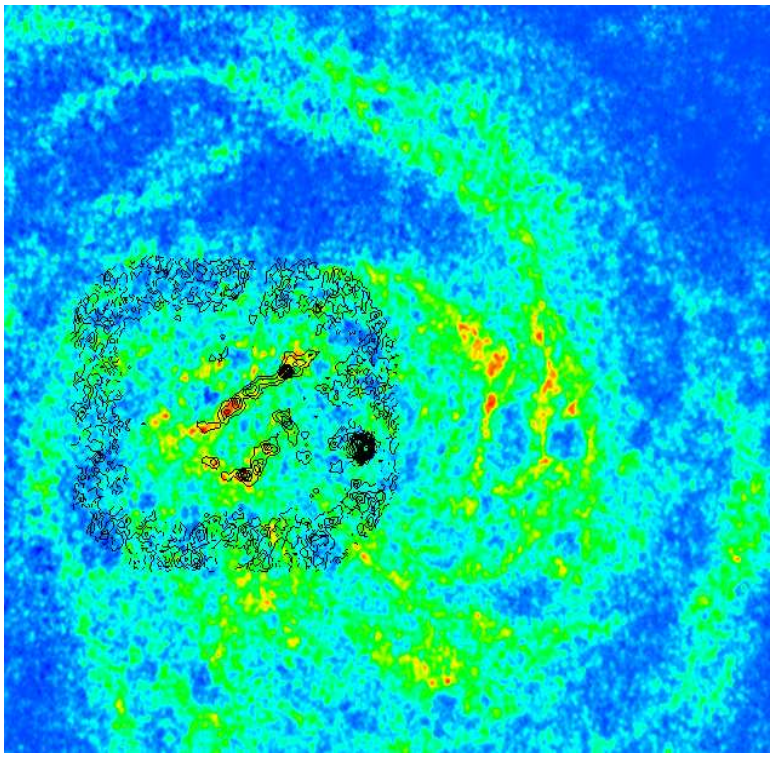

Fig. 13.— Same contour $^{12}$CO map shown in Figure 12, overlaid on a HI image from THINGS.

## 7. Jonathan P. Seale (University of Illinois)

## Detecting Rotation in High-Mass Prestellar Cores

### 7.1. Introduction

Although recent work has led to revolutionary advances in the study of star formation over the last few years, one of the most fundamental questions – the nature and role of magnetic fields during the collapse process – remains largely unanswered. In the case of ambipolar diffusion-driven star formation, the relative drift beteen charged and nautral particles within a cloud core increases the clump's mass-to-magnetic flux ratio via the contraction of neutral particles through the magnetic field lines (Mouschovias 1979). Once this mass-to-flux ratio exceeds a critical value, neutral particles will begin contracting under their own gravity. Due to the effects of magnetic braking during the core formation stage, centrifugal forces are not important to the process. Conversely, in a turbulence-induced star formation model, the turbulent velocity field dominates the magnetic effects and induces fragmentation into high density clumps (e.g. McKee & Ostriker 2007).

Although the predictions of amibipolar diffusion differ in many respects (timescale, spatial distribution, etc.) the differences can be difficult to disentangle observationally. A good test of the two theories – and the importance of magnetic fields – is to probe the rotation of cloud cores. A distinctive prediction of ambipolar-diffusion and magnetic braking theory is a positive correlation between the specific angular momentum and mass of a starless core (Basu & Mouschovias 1995). No such correlation is expected should turbulence dominate the velocity field (Gammie et al. 2003).

We here report the results of a pilot study to detect rotation within prestellar molecular cores. The results of this study can be used as a guide for future observations of more cores with varying properties. Observations and Results are described in the following.

### 7.2. Observations & Results

Observations of a single cloud core were conducted at the Combined Array for Millimeter Astronomy (CARMA; Woody et al. 2004) on 2009 July 15. The array was in the E configuration, the most compact configuration available at CARMA with antenna spacing between 8 and 66 meters. The total on-source time was $\sim 3.8$ hours using the 3 mm receiver with two 2 MHz and 1 500 MHz spectral windows. The frequencies of the to 2 MHz windows were chosen to cover the CS (2–1) line with a rest frequency of 97.980968 GHz.

Observations were conducted of a single high-mass cloud core OrionAN-535254-52433, located within the molecular cloud Orion A North. While lower mass cores have a predicted small rotation velocity ($\sim$ 0.01 km s$^{-1}$) at the size scales probed by the array, higher mass cores are predicted to have azimuthal velocities of $\sim 0.25$ km s$^{-1}$. These velocities are resolveable with the used 63 channels within the 2 MHz bands which provide a velocity resolution of $\sim 0.09$ km s$^{-1}$. Data reduction was performed using MIRIAD.

Figure 14 shows an integrated map of the core over the entire 2 MHz windows which covers the line. We find that the position of the source in the CS map is well-correlated with the core as seen in previous 850$\mu$m

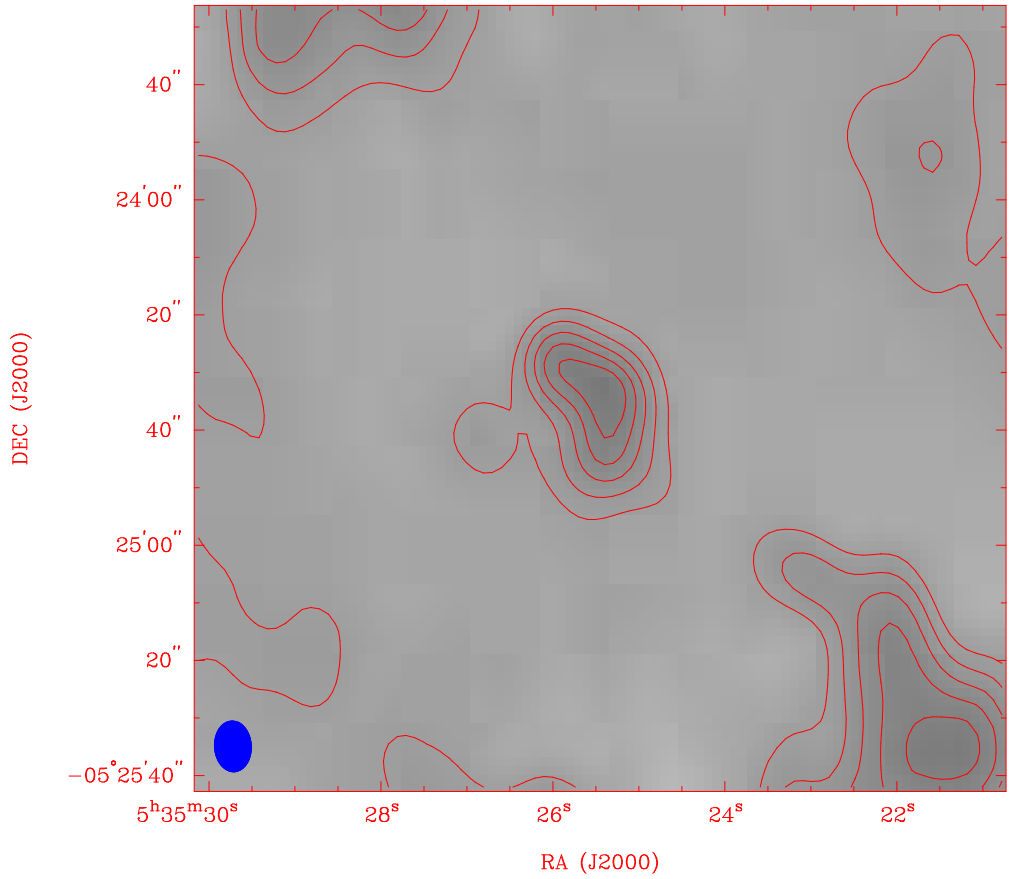


Fig. 14.— Velocity-averaged intensity map of the observed region. Countours are at levels of 0.5*n where n=1,3,5,7,9.

observations(Nutter & Ward-Thompson 2006). The flattened shape of the core is consistent with magnetic field theory which predicts core creation via the flow of material along magnetic field lines.

Figure 15 shows the source in velocity space with each panel showing the source in velocity steps of $\sim$ 0.2 km s$^{-1}$. Note that there appears to be velocity differences between varying areas of the cloud. In particular, there may be a velocity gradient from the lower right to the upper left sections of the cloud. Velocity slices at different points in the core show differences in peak CS line frequency, with variation corresponding to $\sim$ 1 km s$^{-1}$. Such velocity gradients may be the result of core rotation and would represent the first detection of high-mass prestellar core rotation on thi size scale. Further work needs to be conducted to model the clump's structure and rotation to confirm the rotational properties. Using this observation as a guide, a large sample of sources should reveal whether or not a correlation between source mass and specific rotation exists and would illuminate the role of magneitc fields in the core and star formation process.

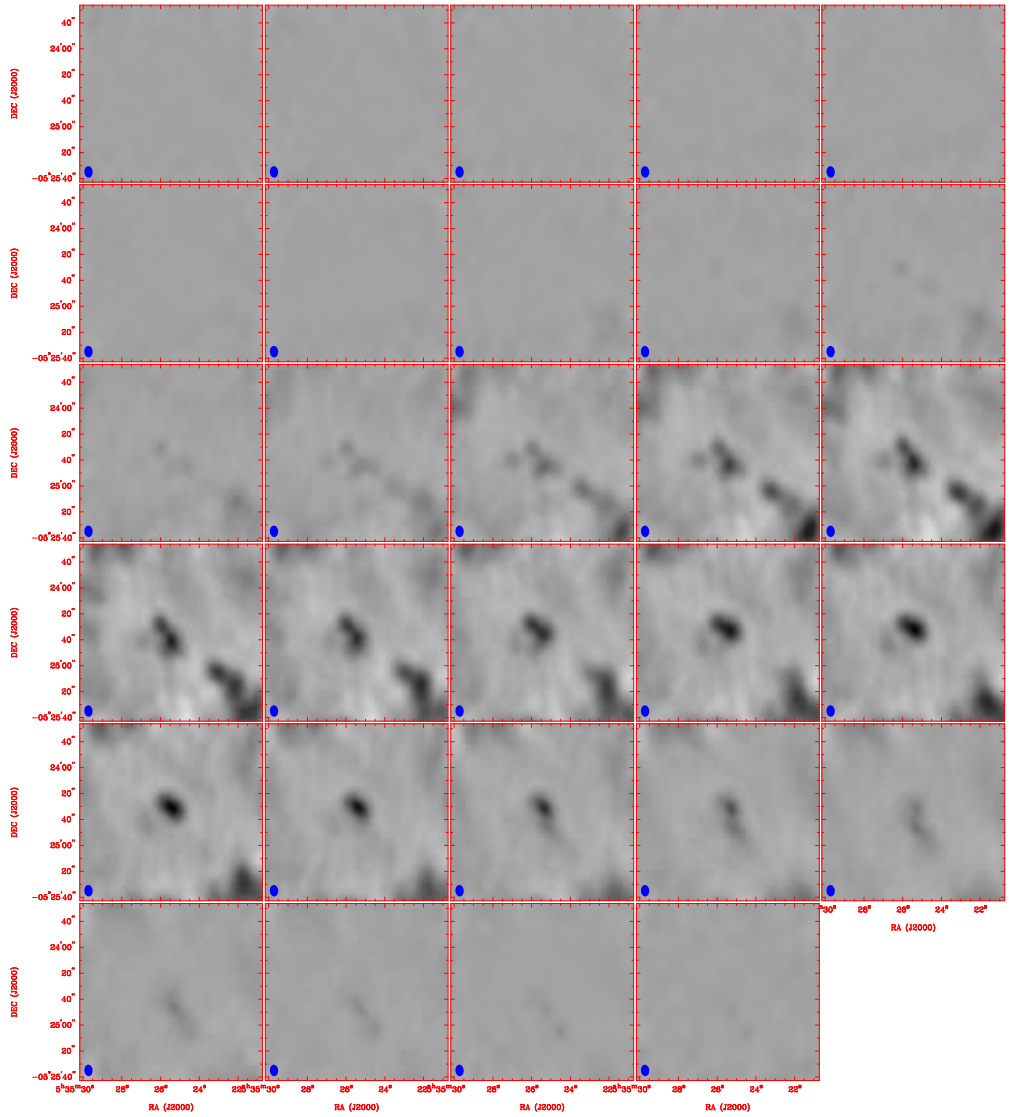


Fig. 15.— Channel maps of the Orion AN source where each panel represents 2 channels (0.2 km/sec) in velocity space.

### 8. Esra Bulbul (University of Alabama in Huntsville)

The Taffy galaxy system UGC 12914/5 is a gas rich interacting galaxy system. The galaxy UGC 12915 passes through the rotating disk of the galaxy UGC 12914 and forms a bright radio synchrotron bridge undergoes a star formation triggered by this interaction (Appleton & Struck 1996; Gerber et al. 1990; Gerber Lamb, & Balsara 1996; Struck 1997). The molecular gas located in the bridge of Taffy system is an ideal candidate for studying the effect of galaxy interactions on the ISM and for understanding star formation induced by galaxy interactions. The highest CO concentration between the two galaxies corresponds to the taffy bridge near the galaxy UGC 12915. Therefore I decided to look for CO (1-0) emission form the companion galaxy UGC 12915. The optical image of the galaxy system UGC 12914/5 can be seen in Figure 16.

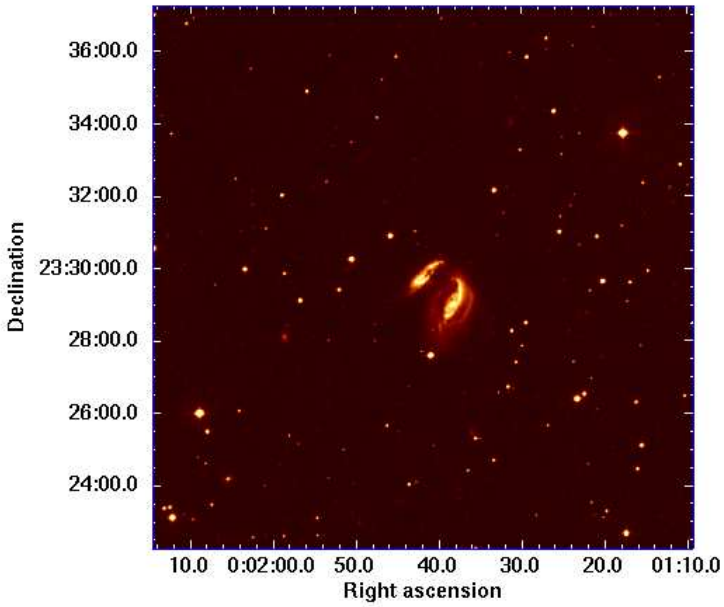


Fig. 16.— SDSS optical image of Taffy galaxy system UGC 12914/5

The observation was taken with CARMA in the E-conguration at 3-mm wavelength. Two narrow band (62 MHz) was used centered on CO(1-0), with one 500 MHz wide bands. The raw visibility data was calibrated using MIRIAD software package. The MIRIAD task INVERT is used to take the Fourier transform of calibrated visibility data. I was able to successfully resolve the CO(1-0) line originated from the taffy bridge and galaxy UGC12915 (see Figure 17).

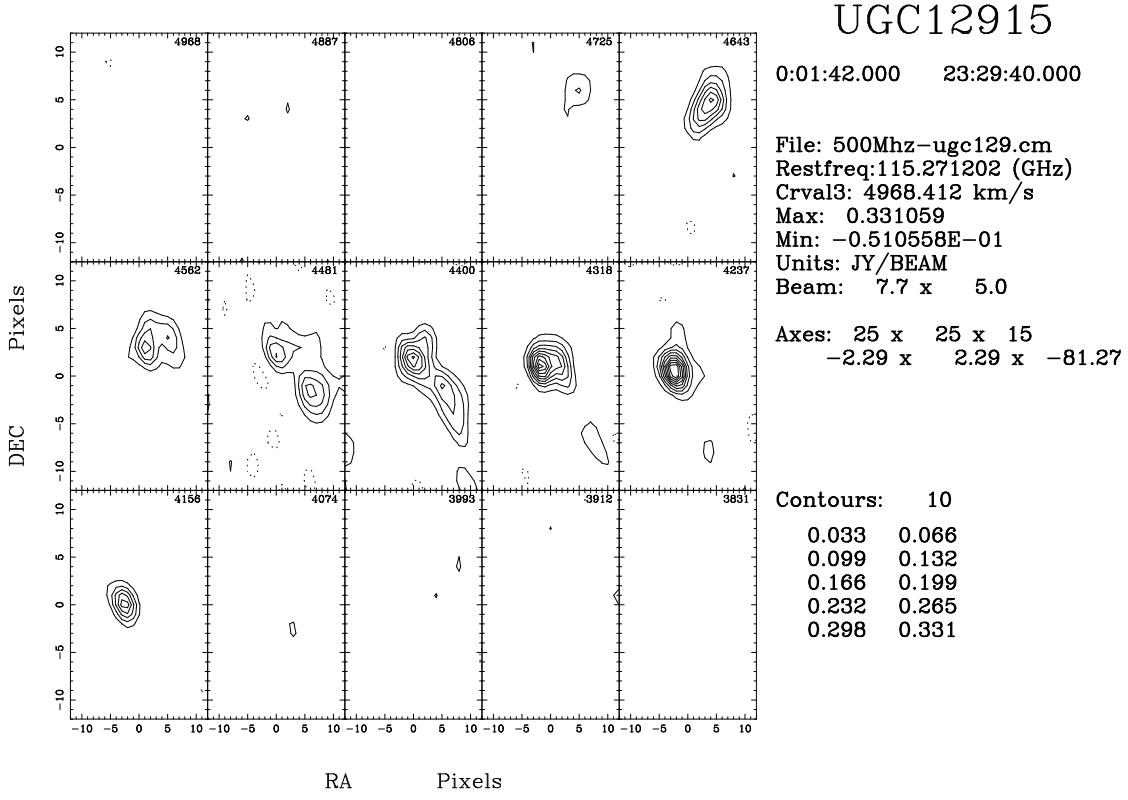


Fig. 17.— The CO(1-0) emssion from galaxy UGC 12915 and the bridge between two galaxies UGC 12914 and UGC12915 detected by CARMA

## 9. Adam N. Morgan (University of California at Berkeley)

### 9.1. Introduction: GRB 090709A

At 07:38:34 UT on July 9th 2009, the Burst Alert Telescope (BAT; Barthelmy et al. 2005) onboard NASA's Swift satellite (Gehrels et al. 2004) triggered on GRB 090709A. The on-board X-Ray Telescope (XRT; Burrows et al. 2005) began observations 67.8 seconds after the trigger, and detected an uncataloged X-ray source which was determined to be the X-ray afterglow of the GRB (Morris et al., GCN 9625). Ground based robotic telescopes slewed to the GRB position, and NIR observations detected a highly reddened, fading afterglow (Aoki et al., GCN 9634; Morgan et al., GCN 9635). Faint detections in optical wavelengths (Cenko et al., GCN 9646; Guidorzi et al., GCN 9648) combined with high energy BAT/XRT analysis (Butler, GCN 9639) indicate that the reddening was due to extinction rather than high redshift. The probable low-redshift nature of this event, combined with a lack of host galaxy detection in deep optical images (Castro-Tirado et al., GCN 9655) and the first ever quasi-periodic oscillations seen in a classical GRB (Markwardt et al. GCN 9645, Golenetskii et al. 9647, Gotz et al. GCNC 9649, Ohno et al. GCNC 9653), indicate that this is indeed an unique event, and would benefit from further multi-wavelength observations.

### 9.2. CARMA Observations of GRB 090709A

We observed the field of GRB 090709A with the Combined Array for Research in Millimeter-Wave Astronomy (CARMA) at an average frequency of 88.5 GHz beginning at 2009-07-15 04:41:33 UT, 5.88 days after the Swift trigger. No source was detected at the position of the NIR/optical afterglow down to the following limits:

| post_burst | | | | |
|---|---|---|---|---|
| t_mid(d) | exp(h) | freq_mid(GHz) | bandwidth(MHz) | flux (mJy) |
| 5.98 | 3.79 | 88.5 | 3000 | < 1.1 (3 sig) |

The quasar 1849+670 was used as a phase calibrator, and fluxes were calibrated to an observation of Neptune taken at the end of the track. The results of this observation have been distributed via the Gamma-ray Burst Coordinates Network (Morgan et al., GCN 9685).

### 9.3. Curiosities with Quasar 1849+670

During the calibration and reduction of the GRB data, a significant ($\sim$ 10%) variation in the uncalibrated flux of our phase calibrator, the bright quasar 1849+670, was observed over the course of the night (Figure 18). This variation was observed in all baselines and was not present in observations of a second quasar (1955+515) taken over the same time period. A plot of the dirty map and beam of 1849+670 shows that the source is indeed point-like (Figure 19), ruling out extended emission as the cause. The non-variation of

1955+515, along with a plot of amplitude versus elevation for the two sources (Figure 20) seems to rule out atmospheric effects as the cause of the change in flux. The strongest correlation seems to be with parralactic angle (Figure 21). While other possible causes for the variation cannot be completely ruled out, polarization of the source on the order of 10% seems most consistent with these relationships. We note that such a level of polarization is high for mm wavelengths.

We thank the staff and observers at CARMA and instructors of the CARMA Summer School for excellent support during the observations and analysis.

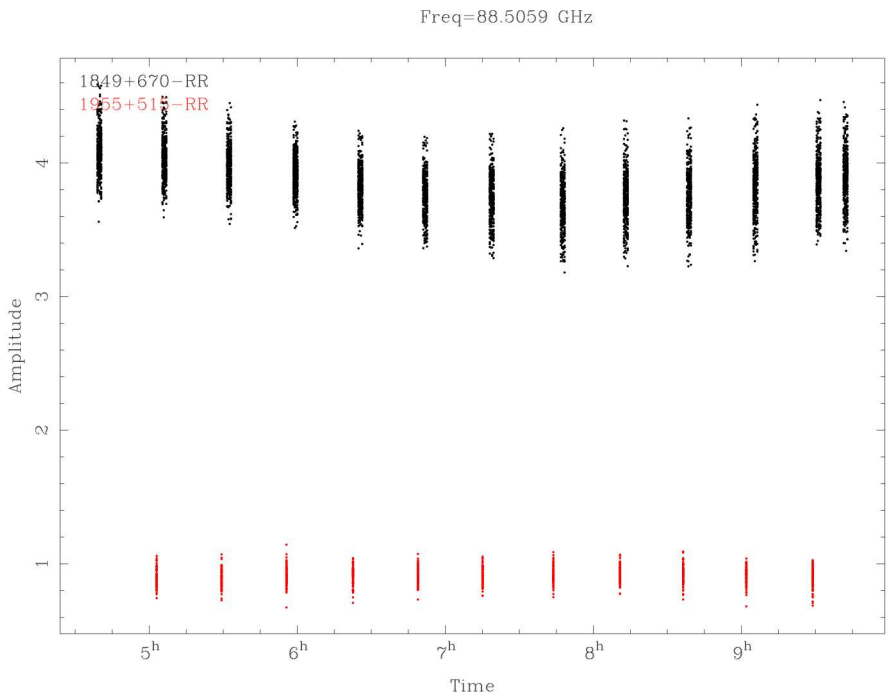


Fig. 18.— Amplitude vs. Time for 1849+670 and 1955+515. The bright quasar 1849+670 shows a $\sim$ 10% variation in flux over the observation which is not seen in 1955+515.

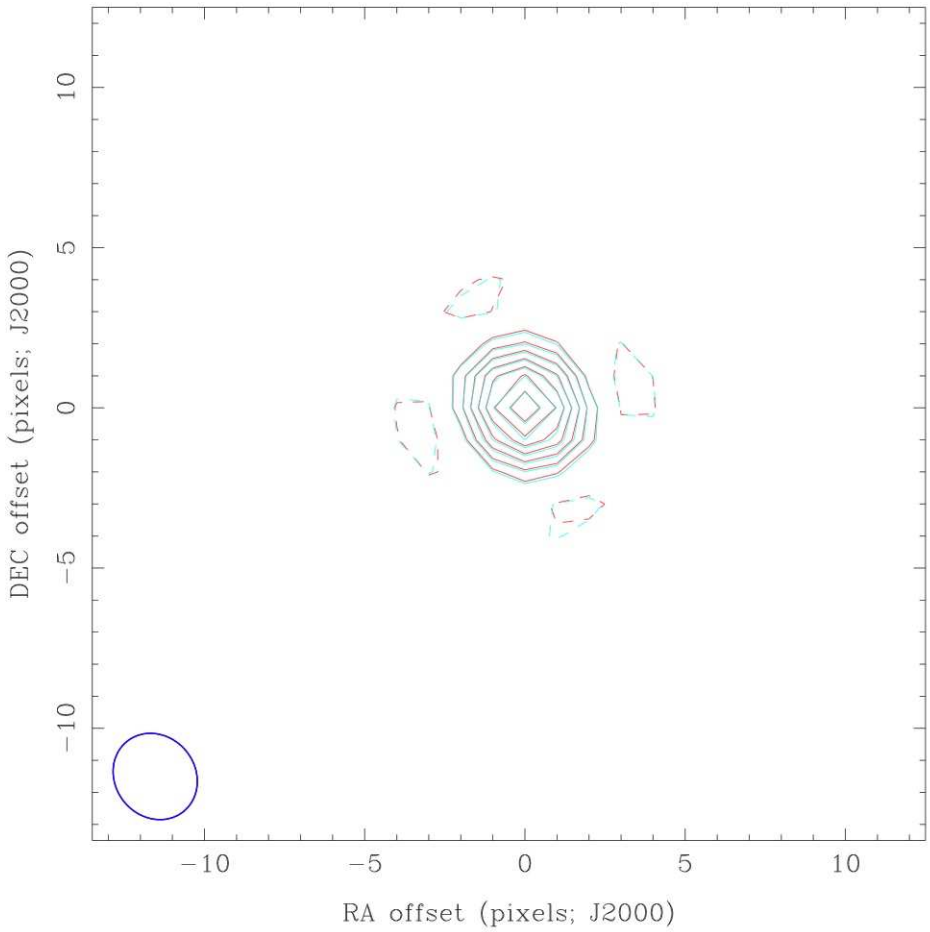


RA, DEC, FREQ = 18:49:16.072, 67:05:41.68, 8.52715098E+01 GHz at pixel (14.00, 14.00, 1.00)
Spatial region : 1,1 to 26,26 Spectral inc/bin : 1/1 =1.294/1.294 (GHz)
Contour image: 1849+670.map (1849+670) Min/max=−0.7793/4.077 JY/BEAM
Contours : −0.5141, 0.5141, 1.028, 1.542, 2.056, 2.57, 3.085, 3.599, 4.113
Contour image: 1849+670.beam (1849+670) Min/max=$10^{30}$/$-10^{30}$ JY/BEAM
Contours : −0.125, 0.125, 0.25, 0.375, 0.5, 0.625, 0.75, 0.875, 1

Fig. 19.— Dirty Map (red contour) and Beam (cyan contour) for 1849+670, indicating that the source is indeed point-like.

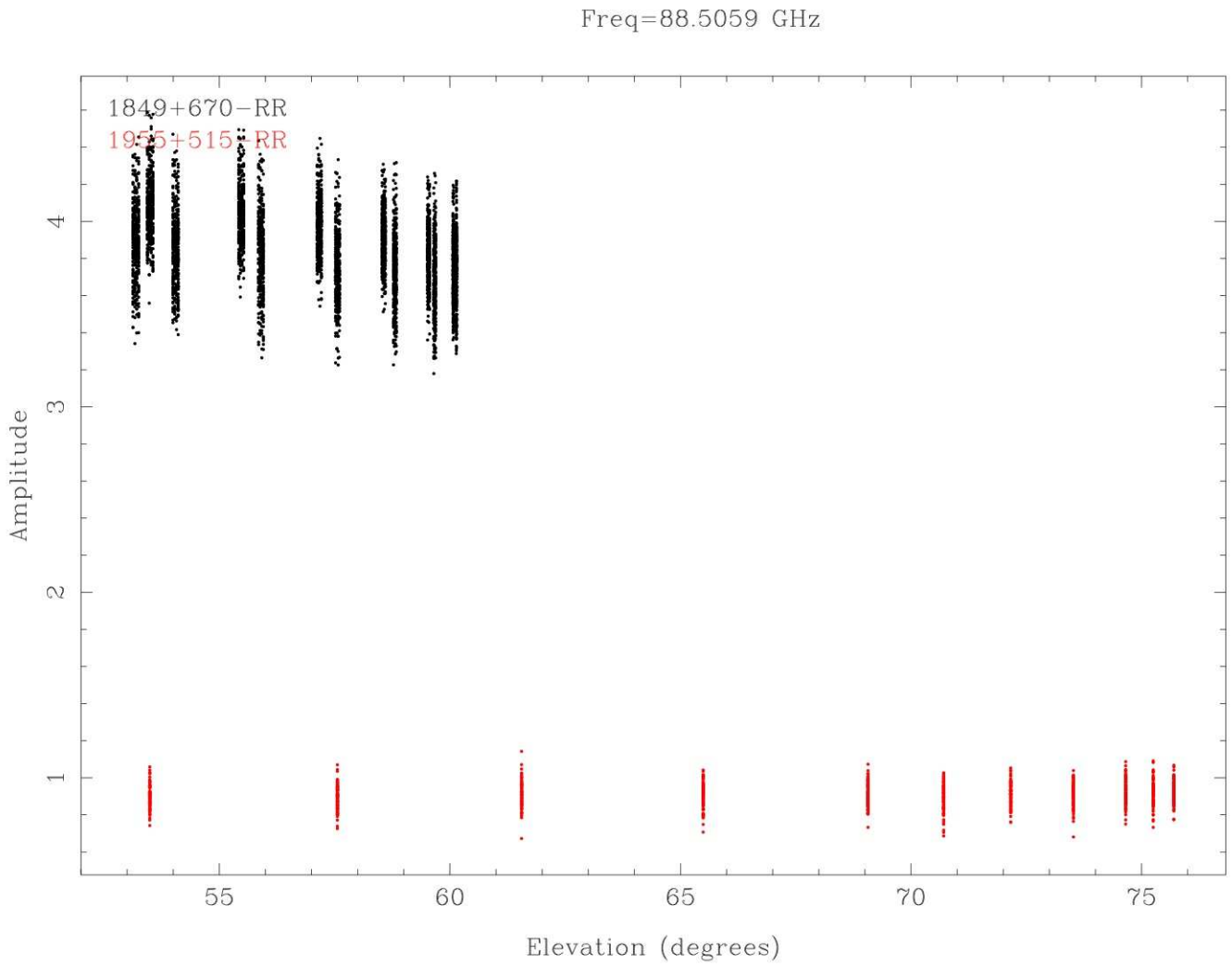


Fig. 20.— Amplitude vs. Elevation for 1849+670 and 1955+515. While there is an inverse relationship between the brightness of 1849+670 and its elevation, the "stepwise" behavior seen in the flux at roughly identical elevations (corresponding to when the source was rising and setting, respectively), indicates that position in the sky is not the only culprit. Note also no change in flux for 1955+515 over the same elevations.

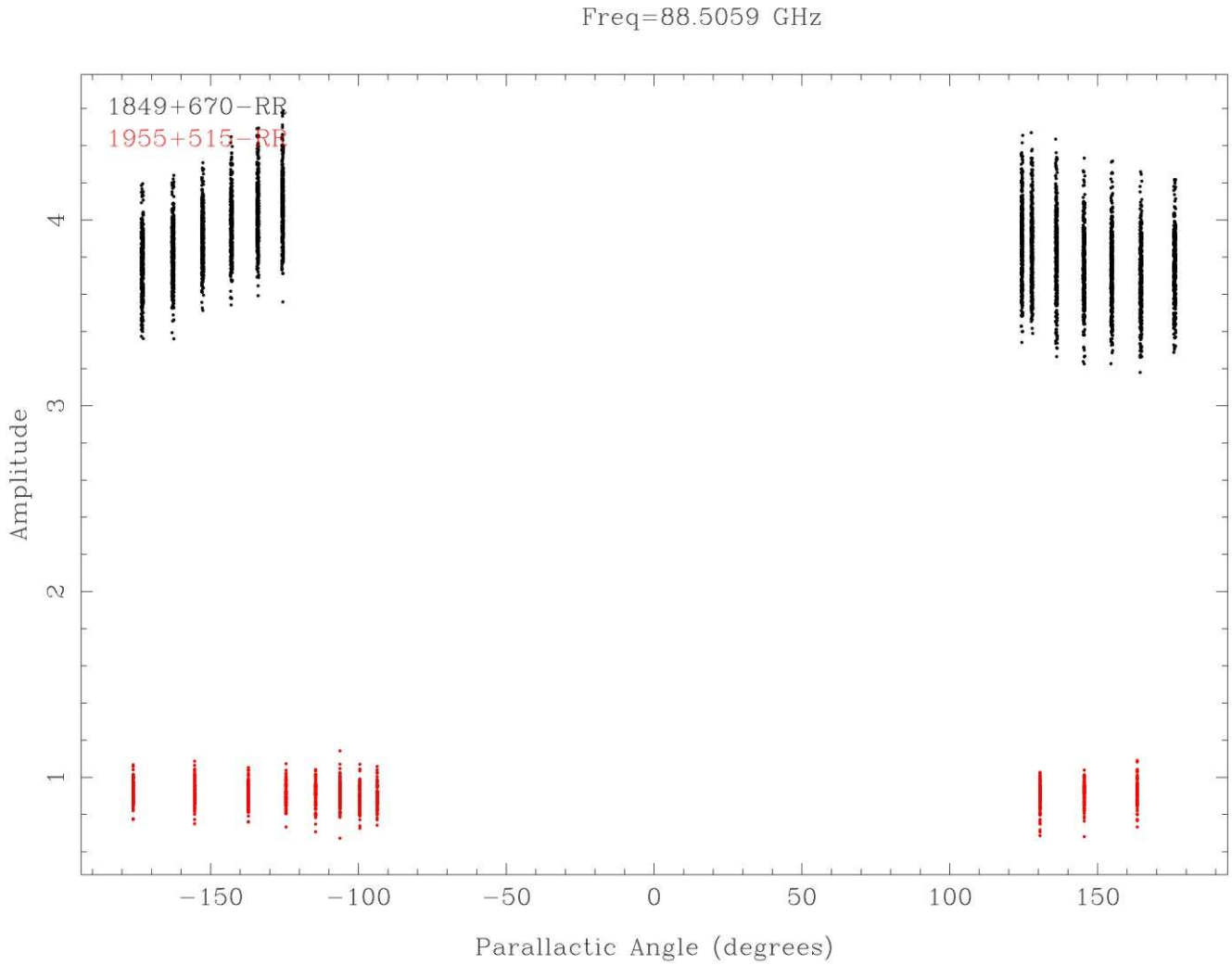


Fig. 21.— Amplitude vs. Parallactic Angle for 1849+670 and 1955+515. A strong relationship is seen in the flux of 1849+670 as a function of parallactic angle. This seems to imply that the change in variation could be due to the source being polarized at the level of $\sim$ 10%.

## 10. Shaye Storm (University of Maryland)

I observed NGC3773, which is a star-forming, early-type lenticular galaxy. The galaxy has been observed as part of the Spitzer SINGS campaign, as well as with the CARMA C- and D- array configurations. It has an optical disk of 1.0 by 1.2 arcsec (Bendo, 2007) and a VLSR of 987 km/s. The preliminary CARMA data revealed two distinct CO(1-0) blobs separated in space and velocity, which suggests that the origins of gas in this galaxy might be interesting to study. My summer school observations aimed to successfully detect the galaxy in E configuration to complement the higher resolution data, and see if the galaxy has more diffuse CO(1-0) structure.

The galaxy was observed with one 500 MHz band centered on the CO(1-0) line and two overlapping 62 MHz bands offset by approximately 6 channels from the line. We used a 7 pointing mosaic, but learned after data reduction that the galaxy has an approximate diameter of 10 by 15 arcsec in this wavelength regime. Knowing that, it was unwise to use a mosaic, and we could have saved time by not pointing off center. We observed 3C273 as the bandpass and phase calibrator. We observed the source and calibrators for 5.0 hours total, but were terminated 40 minutes prematurely when the generator failed. The late afternoon weather made for a high sky rms, and the overall track grade was a C.

During the data reduction, we average four 2.54 km/s channels together to increase signal to noise. We detected the galaxy at the center of our image at the predicted velocity range. Figure 22 shows the galaxy in four velocity channels in our E configuration, with D configuration data overlaid in contours. The E configuration data on the 983 km/s map has a total flux of 0.147 Jy and an rms of 0.0336 Jy, giving us a four sigma detection. The D configuration data on the map has a total flux of 0.203 Jy and an rms of 0.0187 Jy.

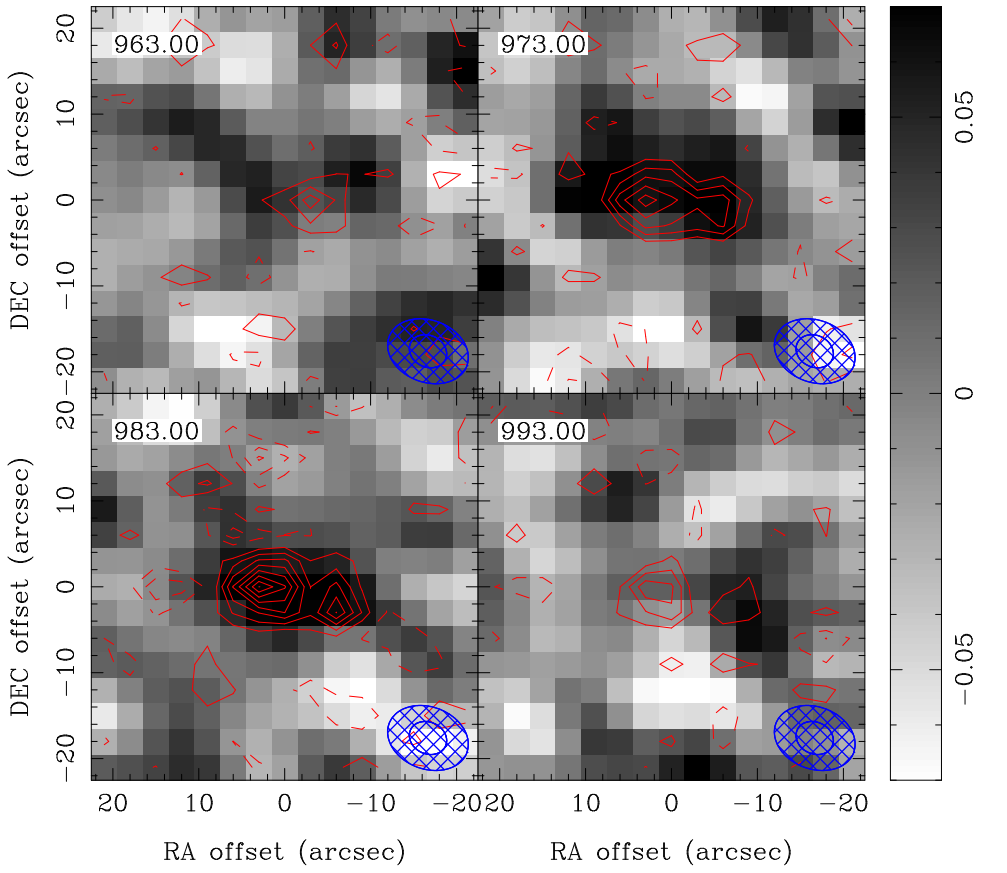


RA, DEC, VELO = 11:38:12.990, 12:06:43.40, 8.63000E+02 km/s at pixel (48.00, 47.00, 1.00)
Spatial region : 41,40 to 55,54 Spectral inc/bin : 1/1 =10/10 (km/s)
Pixel map image: co_2.sdicm (NGC3773) Min/max=−0.08403/0.0716 Range = −0.07 to 0.07 JY/BEAM (lin)
Contour image: Dconfig (N3773) Min/max=−0.01725/0.03259 JY/BEAM
Contours : −0.04267, −0.03414, −0.0256, −0.01707, $-8.534\times10^{-3}$, $8.534\times10^{-3}$, 0.01707, 0.0256, 0.03414, 0.04267, 0.05121, 0.05974, 0.06827

Fig. 22.— CO(1-0) emission from galaxy NGC3773. Pixels represent E configuration data, and contours represent D configuration data.

## 11. Tucker Jones (California Institute of Technology)

### 11.1. Introduction

The peak epoch of galaxy and star formation in the universe occured at redshifts $z = 2-3$. Star formation is fueled by massive reservoirs of cold molecular gas, most easily traced by CO emission at millimeter wavelengths. Millimeter observations will therefore play a key role in understanding the formation and evolution of present-day massive galaxies at early times. However, the expected luminosity of CO emission lines is beyond the capabilities of current facilities for all but the most extreme sub-millimeter and gas-rich QSO populations at high redshift. Fainter objects can be observed in cases of strong gravitational lensing, where the flux of a background source may be amplified by a factor of 20 or more. Herein I report observations of the rich galaxy cluster Abell 2218 which demonstrate the power of lensing to detect intrinsically faint objects. Abell 2218 is an excellent target with at least three strongly lensed galaxies at a common $z = 2.52$ (Kneib et al. 2004), at least one of which shows strong CO emission (Sheth et al. 2004).

### 11.2. Observations and Results

Observations of the lensing cluster Abell 2218 were carried out with CARMA in the E configuration on 16 July 2009. Three 500 MHz correlator bands were used to search for CO(3→2) emission at $z = 2.52$ as well as CO(1→0) at $z = 0.179$, the cluster redshift. The frequency range observed was 97.52–98.92 GHz (single side band). Abell 2218 was observed with single pointings centered at ($\alpha$, $\delta$) = (16:35:51.40, +66:12:44.70) for a total integration time of 1.65 hours in reasonable conditions (6.0–7.5 mm precipitable $H_2O$ and $\tau_{230} = 0.4$–$0.65$). The MIRIAD software package was used to calibrate and image the visibility data.

The brightest sub-millimeter source at $z = 2.52$ was detected in CO(3→2) emission. Figure 23 shows an optical image of Abell 2218 with contours of intensity at 98.3 GHz, the redshifted line frequency, with a $3\sigma$ intensity peak nearly coincident with the brightest lensed image of SMM J16359+6612. Figure 24 shows the extracted spectrum of this source which exhibits a broad (FWHM $\sim 400$ km s$^{-1}$) emission feature with integrated intensity $S_{CO} = 4.0 \pm 1.8$ Jy km s$^{-1}$. There is an additional $\sim 20\%$ uncertainty in absolute flux calibration, since this was done with observations of the gain calibrator rather than a standard flux calibration source. The flux is consistent with the value $3.5 \pm 0.12$ found by Sheth et al. (2004). For a lensing amplification factor $\mu = 22$ they determine a total $H_2$ mass $\sim 0.5 - 2 \times 10^{10}$ M$_\odot$.

No other $z = 2.52$ sources were detected down to a $3\sigma$ sensitivity limit of 20 mJy for 95 km s$^{-1}$ bins, and no cluster members were detected in CO(1→0) emission within $\pm 1000$ km s$^{-1}$ of the cluster redshift. The $3\sigma$ sensitivity corresponds to an upper limit on molecular gas mass of $\lesssim 3 \times 10^8$ M$_\odot$ for cluster members.

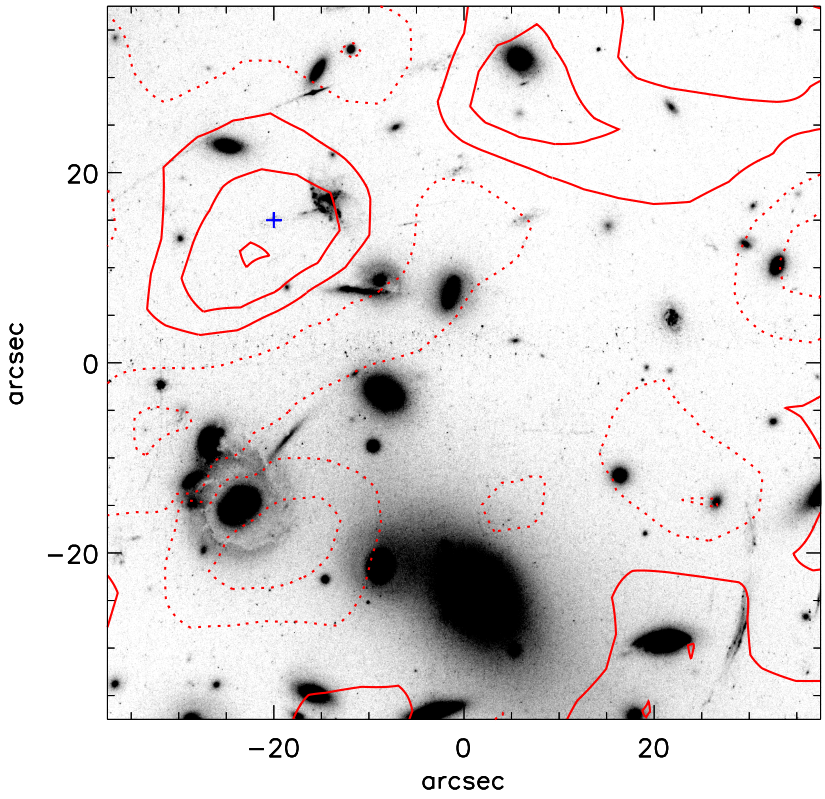


Fig. 23.— HST ACS F555W image of Abell 2218 with CO contours. Contour levels are ±1,2,3σ intensity (dashed lines are negative) integrated over $\Delta v = 300$ km s$^{-1}$ about the redshifted CO(3→2) frequency. The blue cross shows the optical position of a lensed $z = 2.52$ sub-millimeter galaxy, approximately coincident with a 3σ peak in flux.

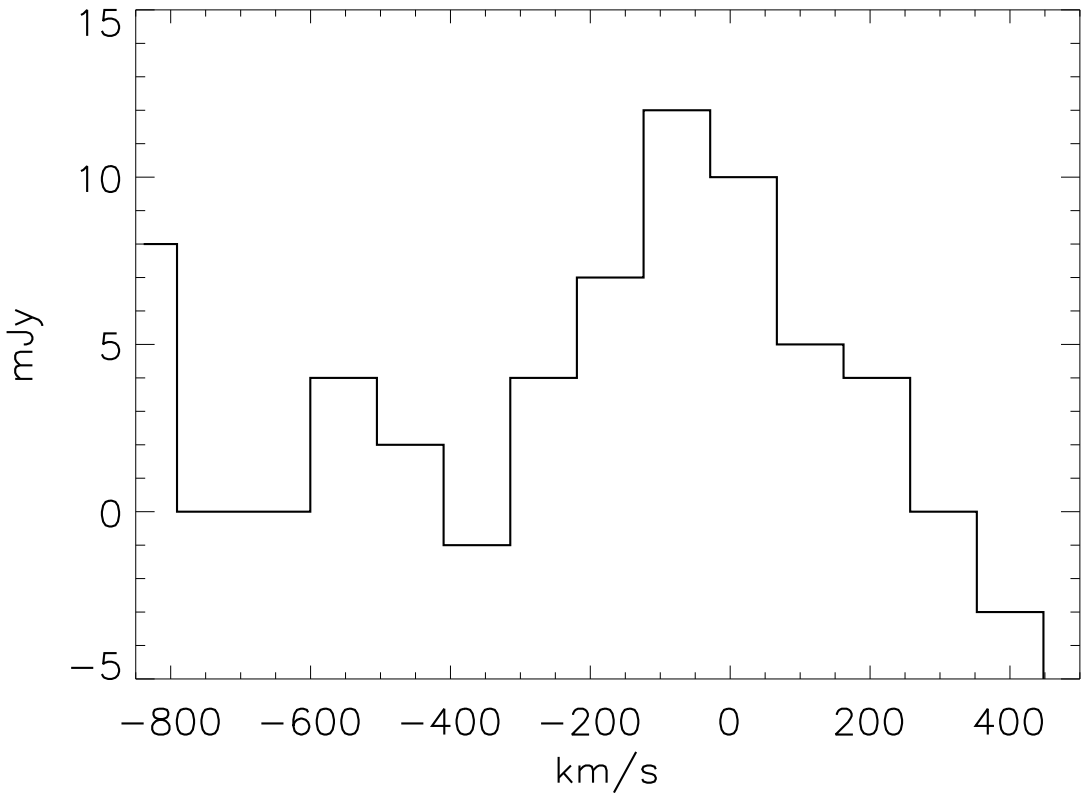


Fig. 24.— Extracted spectra of the sub-millimeter galaxy marked in Figure 23, showing a broad emission feature. Velocity is relative to the expected CO(3→2) line center.

## 12. Laura Lopez & Nurur Rahman
## Star Formation Properties in the Disk of NGC 4254 (M99) Using Various Tracers of Molecular Gas

### 12.1. Introduction & Motivation

Current studies of star formation (SF) properties in galaxy disk use either CO J=1-0 emission map which traces cold diffuse molecular gas or HCN emission line which trace warm high density molecular gas. The emerging picture is that studies of star formation one should be using high density gas tracers (e.g. HCN, HCO+) which correlates better with the star formation tracers such as UV, Halpha, or mid-IR 24 micron emission (Gao & Solomon 2004; Kennicutt et al. 2007). However, the outcome of these studies are somewhat ambiguous since to date there is no systematic study of SF law using various gas density tracers which could provide strong evidence in favour of the emerging picture or disprove it.

### 12.2. Proposed Observation

In this CARMA summer project we are proposing to observe M99 at 89.5 GHz to construct HCN and HCO+ emission line maps. Our main interest to study the star formation law in the disk of M99. We have NMA CO J=1-0, IRAM CO=2-1 and JCMT CO J=3-2 observation for the galaxy where the each of these single dish observations has comparable (FWHM 14 arcsec) resolution. Adding CARMA E-array (FWHM 10 arcsec) HCN and HCO+ observations will be extremely useful for our study to better understand the SF property .

### 12.3. Observing Run

We prepared the observing scripts such that the HCN and HCO+ lines were placed in the lower sidebands. The correlator configuration was 500 MHz, 62 MHz, and 500 MHz, respectively, for band 1, 2 and 3. The HCN line was centered on both band 1 and 2 where band 1 had been used to detect the continuum. The HCO+ line had been placed at the center of band 3. We have used 7-point mosaic for the observation with 3 minutes on source integration. The total length of the observing track was 10 hours.

### 12.4. Data Reduction

We have reduced the data using the MIRIAD package. Figure 25 shows the UV coverage for our observation. The HCN and HCO+ emmission line maps had been contstructed from the UV data (Figure 26).

### 12.5. Results

The HCN and HCO+ line emissions are harder to detect for galaxies that are considered normal ($\sim 10$ $M_\odot$ $yr^{-1}$) in forming stars in its disk compared to starburst galaxies that goes through a phase of vigorous star formation ($\sim 100 - 1000$ $M_\odot$ $yr^{-1}$). The disk average SF for M99 is ($\sim 4$ $M_\odot$ $yr^{-1}$) derived from both H$\alpha$ and far-infrared emission maps. Therefore, it was not entirely surprising that we did not get any significant detection in individual line maps for the allotted time. However, when we combined the HCN and HCO+ line emission maps we get 3$\sigma$ detection at the extended tail of the galaxy in the SW direction.

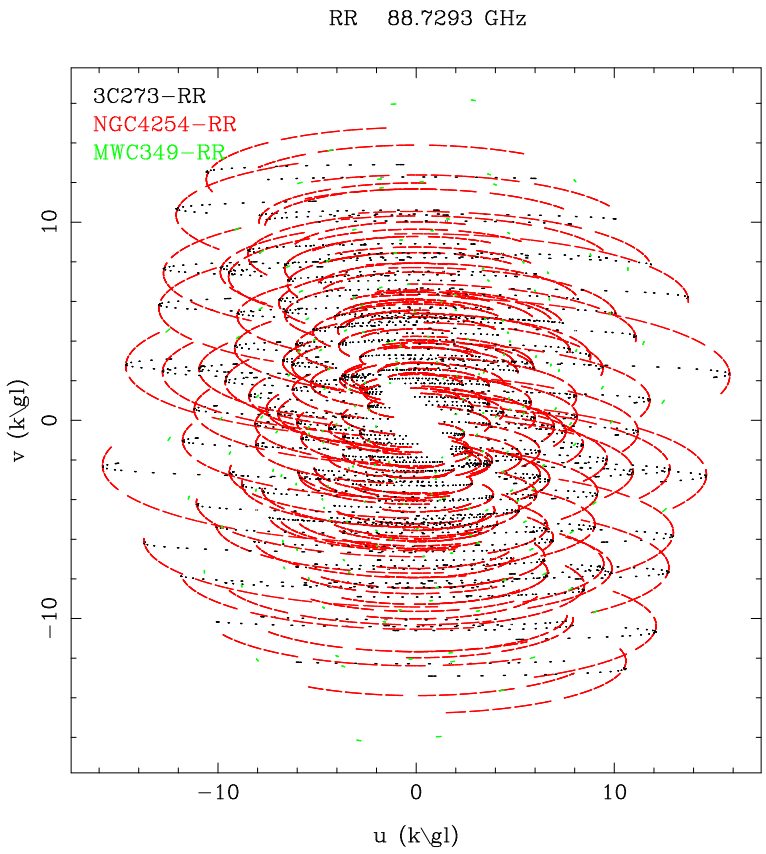


Fig. 25.— UV coverage for M99 observation (in red).The phase and flux calibrators are shown in black and green.

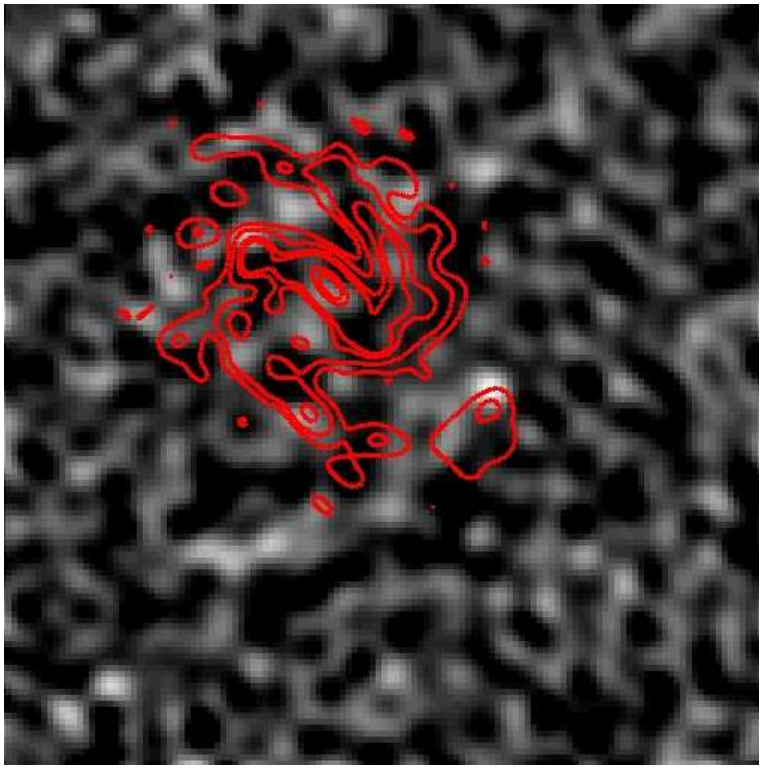

Fig. 26.— HCN+HCO image with CO J=1-0 contour (in red) overlaid. We have noted 3σ from a localized region in the SW direction from the galaxy center. This region is well within the optical radius. This is an interesting observation because CO J=1-0 emission is relatively weak in that region of galaxy disk.

## 13. Alissa Bans (University of Chicago) & Joanna Bulger (University of Exeter)

### 13.1. Motivation

Observations of debris and accretion disks around young stellar objects provide important diagnostics in the testing of theoretical disk models. Millimeter observations are particularly important since they shed light on the mass and surface density of theses disks. In fact, there are already notable millimeter observations of class II accretion disks that have taken advantage of CARMA's unprecedented resolution in the B and C configurations, that have provided constraints on disk models (Isella, Carpenter and Sargent 2009).

Since the telescope during our time at the summer school was in the most compact, E configuration (which has a much larger beam size than the B and C configurations) we chose to observe a class I accretion disk. The motivation being that class I disks are still very young and are therefore more likely to have extended envelopes. The E configuration enables these envelopes and other possible extended features to be detected, such as outflows, that could otherwise be over-resolved and missed in the higher resolution B and C configurations.

The class I object that we chose to observe was IRASF04113+2758, in the Taurus molecular cloud. This object was previously observed by Motte & Andre (2001) at 1.3 mm with the IRAM 30 m telescope with an 11" beam. They concluded that the source was most likely extended and measured a flux per beam of 410 mJy/beam. We concluded that because of this high flux level at 1.33 mm and the nature of class I objects, 4113+2758 would be a good n bright enough source to observe at 3 mm. Our goal was to both verify the presence of an extended envelope and also check for possible outflows.

### 13.2. Observational Details

We devoted two 500 MHz bands to observations of 3 mm continuum and one narrow, 31 MHz band to the $^{12}$CO line (a common tracer of outflows) at $\nu \sim 115$ GHz. The total integrated observing time we spent on the source was 3.5 hours. During our observation antenna 2 had bad amplitude and phase velocity value, we therefore flagged all data from this antenna upon our data reduction. Antennas 5, 6, 7 and 8 had phase errors within one of the 500 MHz continuum bands, which subsequently lead to this data also being flagged.

### 13.3. $^{12}$CO Outflow Results

Figure 27 shows the raw data per channel from the 31 MHz band. Here we have plotted the spatial distribution (RA, DEC) of $^{12}$CO for several o the 126 channels were the flux was the brightest. The associated velocities are shown in the top left corner of each graph. The detection of $^{12}$CO in the raw data is very strong and there is a very noticeable progression across these channels, going from blue shifted $^{12}$CO in the southwest region, to bright central line $^{12}$CO in the central region, to red shifted $^{12}$CO in the northwest region.

Figure 28 shows the contours for both the red shifted and blue shifted $^{12}$CO data, plotted on top of the continuum. .The alignment of the $^{12}$CO data with the centre of the continuum is very convincing of the fact that 4113+2758 has an outflow.

### 13.4. Continuum Results

Figure 29 shows amplitude vs. UV distance for the 4133+2758 continuum. The clear drop in amplitude with UV distance shows that we have resolved the entire extended continuum source. We performed the IMFITS routine on the data and found the size of the continuum source to be 9.3”$\times$5.2” (where as our projected beam size was only 7.8”$\times$3.15”). This rather large size leads us to believe we are seeing an extended envelope of the disk. The total continuum flux from our IMFITS result was 75.3$\pm$7 mJy.

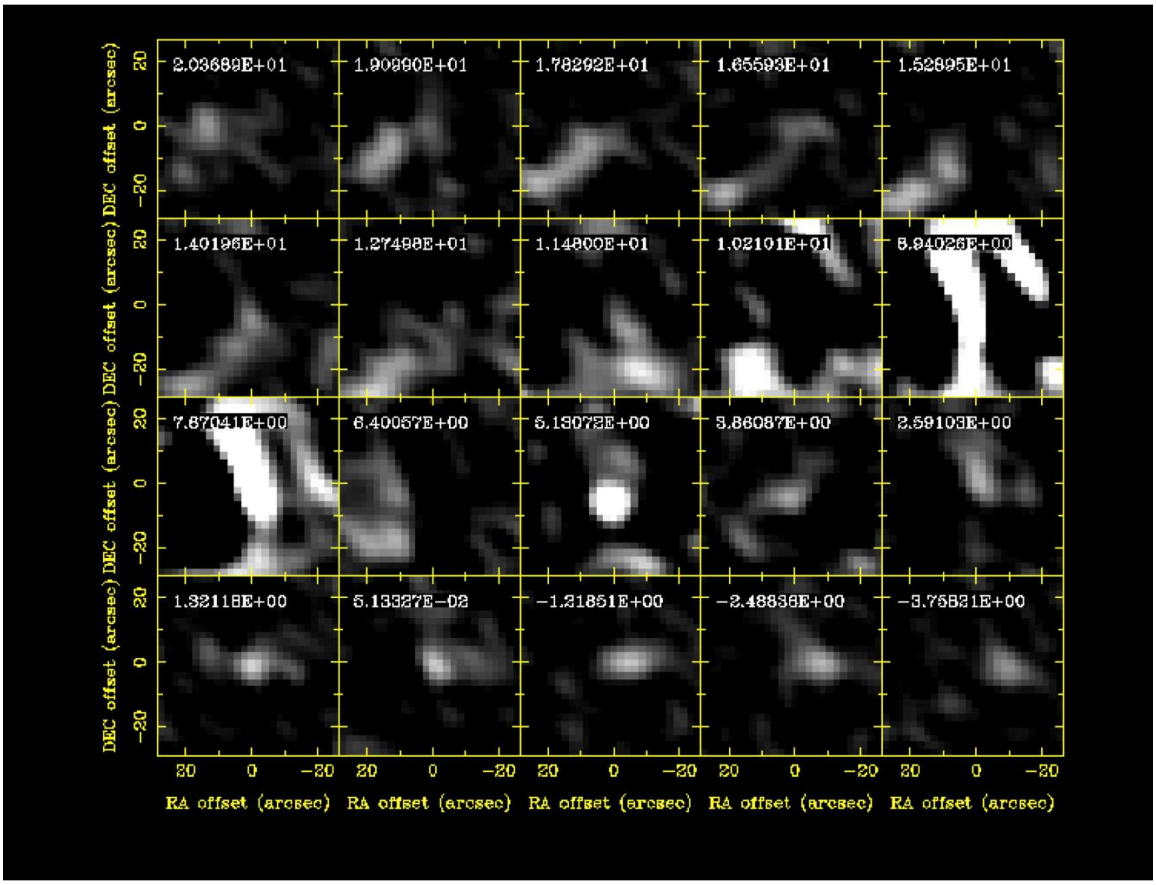


Fig. 27.— Velocity channel maps of $^{12}$CO emission of IRASF04113+2758.

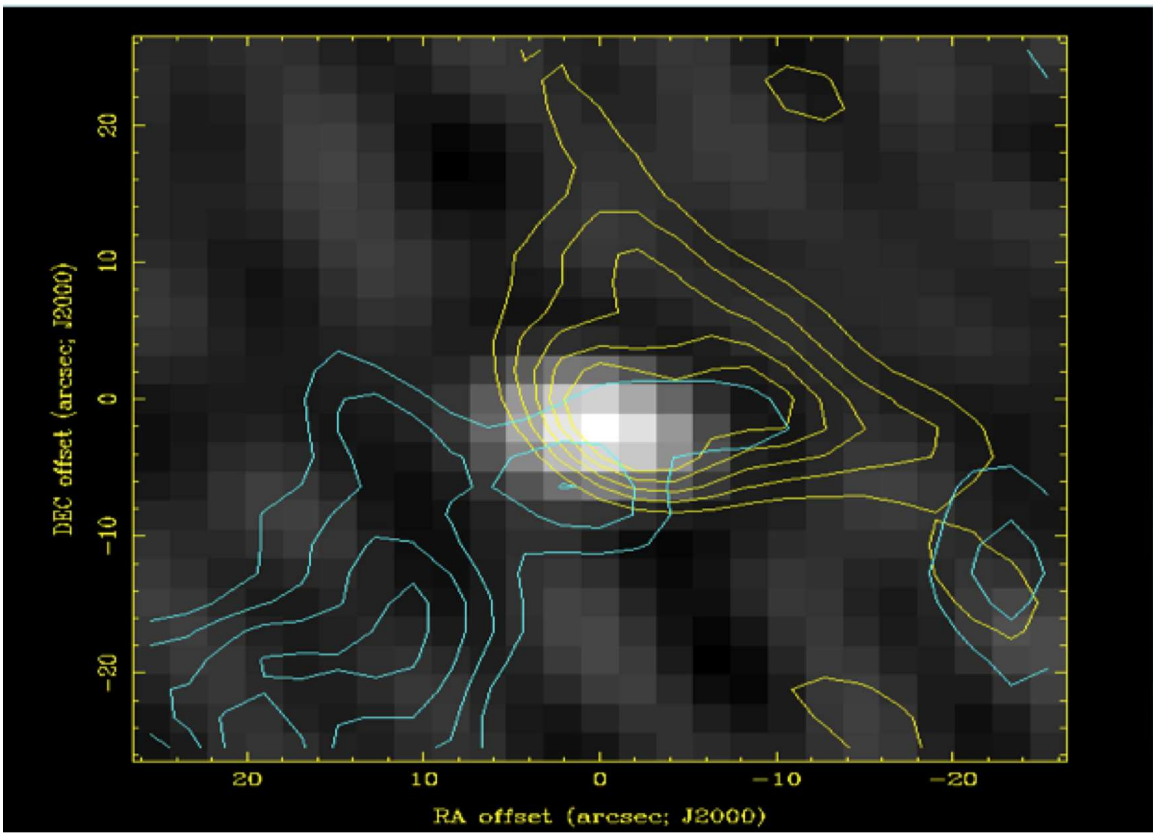


Fig. 28.— Contour map of blue shifted (blue lines) and red shifted (yellow lines) $^{12}$CO emissions of IRASF04113+2758, overlain on the wideband continuum.

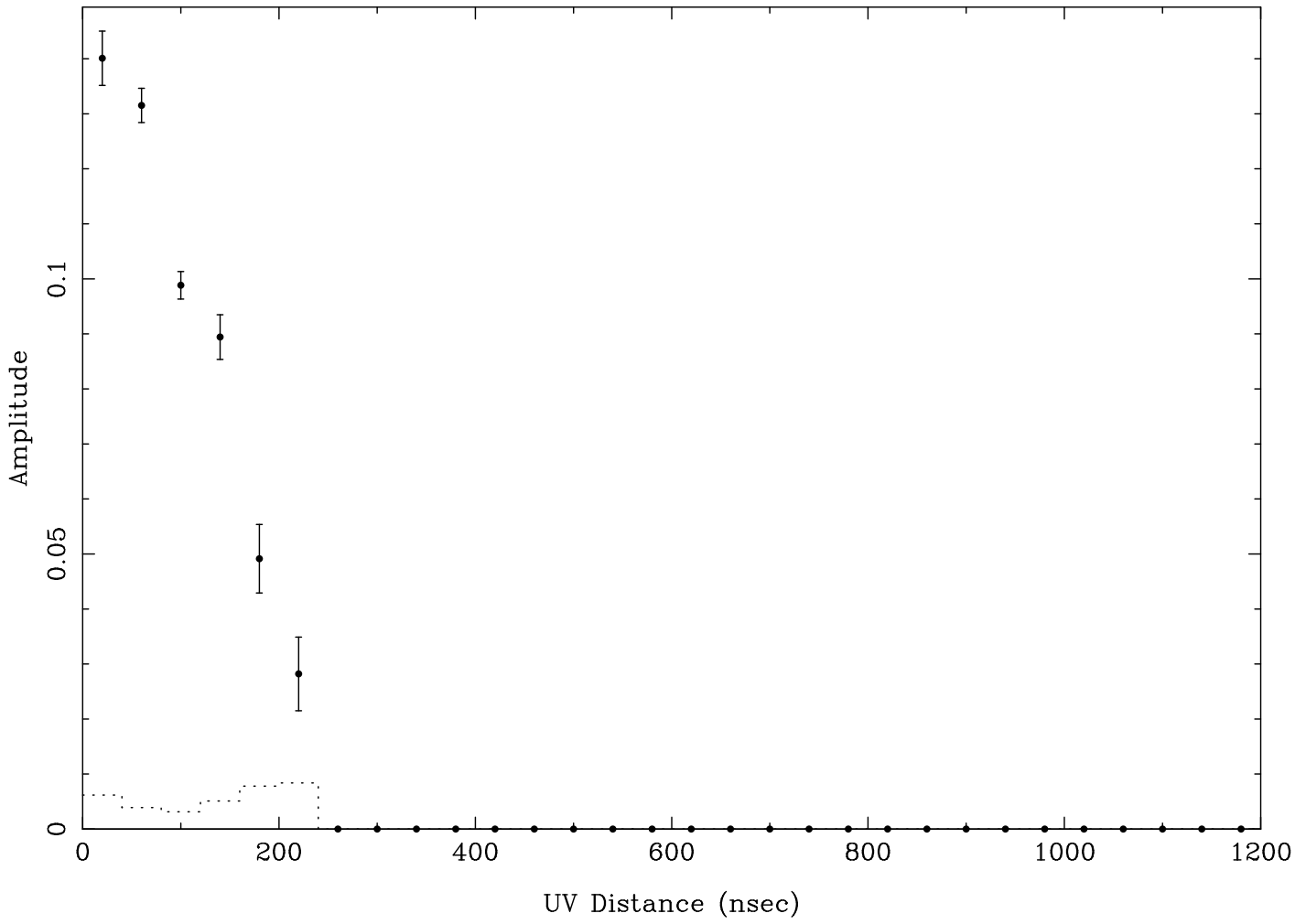


Fig. 29.— Amplitude vs. UV distance in the wideband continuum of IRASF04113+2758.

## 14. Kate Barnes (Indiana University)

### 14.1. Introduction

I am currently studying the recent star formation in the outer disk of a representative sample of 10 nearby spiral galaxies; in particular, galaxies in my sample have been selected to have typical HI disk sizes, i.e., about 1-2$\times R_{25}$. I am using deep, wide-FOV H$\alpha$ imaging and HI maps from the VLA to measure the recent, massive star formation and the underlying neutral gas reservoir for galaxies in my sample. One of my main science goals is to conduct a Toomre stability analysis on the H$\alpha$/UV subsample using both azimuthally averaged surface densities throughout the entire galaxy as well as a point-by-point analysis of individual star forming complexes in the outer disk. To accurately measure the Toomre stability criterion I need to measure the gas surface density from the combined neutral and molecular components. In particular, it is essential to obtain CO maps of the central portions of our galaxies, as this is where the gas is predominately molecular (e.g., BIMA SONG, Helfer et al. 2003). Here, I have conducted observations of the central region of one galaxy from my sample to do a preliminary analysis of star formation regulation.

### 14.2. Observations

I observed the 115GHz CO (1-0) line in NGC1073 using CARMA in E configuration on July 14$^{th}$, 2009. The correlator was configured using one 500MHz band and two 62MHz bands, with the 62MHz bands overlapping by several channels. The IF was set to observe $^{12}$CO in the USB and $^{13}$CO in the LSB. The observations consisted of a 19-point mosaic centered slightly offset from the center of the galaxy; the mosaic covered $\sim$2' in diameter, which corresponds to $\sim 0.6\times R_{25}$. The total time spent on source was 3.2 hours, which was planned to reach a sensitivity of $\sim$45mJy/beam for 10km/s channels. The angular resolution of the observations was $\sim$8".

### 14.3. Results

There were no detections of $^{12}$CO or $^{13}$CO down to the 1$\sigma$ sensitivity level of $\sim$ 60mJy/beam for 10km/s channels. The sensitivity corresponds to a CO intensity of $\sim$1 K km s$^{-1}$, which using a standard conversion of CO intensity to $H_2$ column density corresponds to a column density of $\sim 3\times 10^{20}$ $H_2$ cm$^{-2}$. The only single-dish observations of NGC1073 in the literature report a dubious detection of CO (2-1) of $\sim$ 2 K km s$^{-1}$ (Braine et al. 1993). I will use the upper limit on the surface density of molecular gas within the galaxy in order to further constrain our understanding of star formation regulation in NGC1073.

## E-mail addresses

Berkeley
Chat Hull, chat@astro.berkeley.edu,
Statia Luszcz Cook, sluszcz@astro.berkeley.edu
Adam Morgan, amorgan@astro.berkeley.edu

Maryland
M. Nurur Rahman, nurur@astro.umd.edu
Shaye Storm, UMD, shaye.storm@gmail.com

Illinois
Rui Xue, ruixue1@astro.uiuc.edu
David Andres Rebolledo Lara, dreboll3@astro.uiuc.edu
Jonathan Seale, seale@astro.uiuc.edu

Chicago
Alissa Bans, abans@uchicago.edu
Reid Sherman, ras@uchicago.edu

Caltech
Alex Lockwood, alock@gps.caltech.edu
Shriharsh Tendulkar, spt@astro.caltech.edu
Tucker Jones, tajones@astro.caltech.edu
Lee Rottler, rottler@ipac.caltech.edu

Outside
Gul  Esra Bulbul, gul.bulbul@uah.edu, U of Alabama
Laura Lopez, lopez@astro.ucsc.edu, UC Santa Cruz
Kate Barnes, barneskl@astro.indiana.edu , Indiana University
Joanna Bulger, jmb212@exeter.ac.uk, University of Exeter
Nasirah Jetha, nazjetha@gmail.com, U of Alabama

## REFERENCES

Aoki, K., et al. 2009, GRB Coordinates Network, 9634, 1

Barthelmy, S. D., et al. 2005, Space Science Reviews, 120, 143

Basu, S., & Mouschovias, T. C. 1995, ApJ, 453, 271

Bendo, G. J., & Calzetti, D.& Engelbracht, C. W. & Kennicutt, R. C. & Meyer, M. J. & Thornley, M. D. & Walter, F. & Dale, D. A. & Li, A. & Murphy, E. J. 1995, MNRAS, 380, 1313

Burrows, D. N., et al. 2005, Space Science Reviews, 120, 165

Butler, N. 2009, GRB Coordinates Network, 9639, 1

Carlstrom, J. E., & Kronberg, P. P. 1991, ApJ, 366, 422

Castro-Tirado, A. J., et al. 2009, GRB Coordinates Network, 9655, 1

Cenko, S. B., et al. 2009, GRB Coordinates Network, 9646, 1

Gehrels, N., et al. 2004, ApJ, 611, 1005

Guidorzi, C., et al. 2009, GRB Coordinates Network, 9648, 1

Golenetskii, C., et al. 2009, GRB Coordinates Network, 9647, 1

Gotz, D., et al. 2009, GRB Coordinates Network, 9649, 1

Kneib, J.-P., van der Werf, P. P., Kraiberg Knudsen, K., Smail, I., Blain, A., Frayer, D., Barnard, V., & Ivison, R. 2004, MNRAS, 349, 1211

Markwardt, C. B., et al. 2009, GRB Coordinates Network, 9645, 1

McKee, C. F., & Ostriker, E. C. 2007, ARA&A, 45, 565

Morris, D. C., et al. 2009, GRB Coordinates Network, 9625, 1

Morgan, A. N., et al. 2009, GRB Coordinates Network, 9635, 1

Morgan, A. N., et al. 2009, GRB Coordinates Network, 9685, 1

Mouschovias, T. C., & Paleologou, E. V. 1979, ApJ, 230, 204

Nutter, D., & Ward-Thompson, D. 2007, MNRAS, 374, 1413

Ohno, M., et al. 2009, GRB Coordinates Network, 9653, 1

Olofssen, H., & Rydbeck, G. 1984, A&A, 136, 17

Sheth, K., Blain, A. W., Kneib, J.-P., Frayer, D. T., van der Werf, P. P., & Knudsen, K. K. 2004, ApJ, 614, L5

Woody, D. P., et al. 2004, Proc. SPIE, 5498, 30